FFI Norwegian Defence Research Establishment

23/01815

FFI-RAPPORT

Cracking mechanisms in ceramic armor

– analytical solutions and finite element simulations

Martin Fonnum Jakobsen

Cracking mechanisms in ceramic armor
– analytical solutions and finite element simulations

Martin Fonnum Jakobsen

Norwegian Defence Research Establishment (FFI) 20 December 2023

Keywords
Ballistikk
Beskyttelse
Keramikk
Modellering og simulering
IMPETUS
Materialteknologi
Prosjektiler

FFI report
23/01815

Project number
1680

Electronic ISBN
978-82-464-3505-3

Approvers
Morten Huseby, *Research Manager*
Halvor Ajer, *Research Director*

The document is electronically approved and therefore has no handwritten signature.

Summary

The subject of this report is the physics governing ballistic impact on ceramic plates. The report has several goals:

- Develop FFI's basic knowledge of ballistic impact phenomena.
- Provide a general literature review for anyone interested in learning more about ballistic impact and its relation to contact mechanics.
- Evaluate the usefulness of existing analytical methods that describe the ballistic impact problem. In the long term, the most suitable methods may be used as a first step toward the development of an in-house material model for ceramics.
- Report preliminary ballistic impact simulations in IMPETUS Afea to evaluate its current simulation capabilities.

The first part consists of a detailed literature study of several important cracking mechanisms that may emerge during ballistic loading. In addition, we review analytical models that may form the backbone of a new material model for ceramics subjected to projectile impact. The analytical models capture all of the different crack types observed experimentally.

In the second part, we perform and evaluate concrete ballistic impact simulations in IMPETUS Afea. The simulations are able to capture and describe the specific cracking modes and mechanisms. Yet, in order to calibrate the model, we need to perform several in-house experiments at different scales.

The development of an in-house ceramic material model as well as the calibration of the IMPETUS Afea model seem promising but require more work.

Sammendrag

Overordnet handler denne rapporten om fysikken bak ballistisk støt mot keramiske plater. Rapporten har flere mål:

- utvikle FFIs grunnkunnskap om fysikken som er relevant i ballistiske støt;
- være en litteraturstudie som er relevant for dem som er interessert i å lære mer om ballistisk støt og dets relasjon til kontaktmekanikken;
- evaluere nytten av eksisterende analytiske metoder som forsøker å beskrive ballistiske støt. På lang sikt vil (forhåpentligvis) de mest generelle modellene fungere som et springbrett mot utviklingen av en ny keramikkmodell;
- rapportere om innledende simuleringer av ballistiske støt mot keramikkplater i IMPETUS Afea og analysere programmets styrker og svakheter med tanke på den grunnleggende fysikken.

Rapportens første del består av en detaljert litteraturstudie av de dominerende oppsprekkingsmekanismene som finner sted når et prosjektil treffer en keramikkplate. I tillegg ser vi på analytiske modeller som forhåpentligvis (på lengre sikt) kan brukes til å utvikle en ny materialmodell som egner seg for å beskrive keramikk som blir påført en ballistisk last. De analytiske modellene klarer å beskrive de observerbare oppsprekkingsmekanismene.

I del to av rapporten utfører og evaluerer vi konkrete simuleringer av ballistisk støt mot en keramikkplate i IMPETUS Afea. Simuleringene klarer å fange opp og beskrive sprekkene som dannes, og de korresponderende mekanismene. Vi må allikevel kalibrere keramikkens materialmodell gjennom tilpasning av eksperimenter som bør utføres på forskjellige skalaer.

Både utviklingen av en ny keramikkmodell og kalibreringen av IMPETUS Afea-modellen virker lovende, men krever mer arbeid.

Contents

1 Introduction

Lightweight systems for protection against armor piercing (hard core) small arms threats, are often an ceramic plate (or tile) in combination with composite materials and ballistic fiber backings. The ceramic is an essential component as it is capable of blunting, fracturing, and eroding different types of projectiles due to its high hardness. Yet, the ceramic generally becomes highly fractured locally around the point of impact. Once the ceramic's structure is locally compromised, it provides less protection for subsequent impacts. A simple solution is to use thicker ceramic plates, but due to weight restrictions and decreased soldier and vehicle mobility this is often undesirable. Therefore it is important to find a balanced armor system, that gives sufficient protection without being too heavy. In practice, to keep the ceramic from falling apart when damaged, it is often covered by a composite material such as a glass-fiber composite. The role of the ballistic fiber backing is to absorb kinetic energy and prevent both the deformed projectile and ceramic fragments from perforating the armor. In order to understand how to improve ballistic protection it is essential to increase our understanding of the mechanisms governing the contact and fracture dynamics during ballistic loading.

A long term goal at the Norwegian Defense Research Establishment (FFI) is to develop a model that can capture the essential physics governing ballistic impact on an armor system. Of particular importance is the development of a multi-scale material model that can describe ceramics. A well-behaved ceramic model is of importance for the military and the defense sector, because it enables a calculation that can predict whether a ceramic can defeat or will be defeated by a particular projectile. In principle, the establishment of a high quality material model may supplement and allow for a reduced number of necessary experiments on particular protection equipment. This may be beneficial as experiments on protection equipment can be expensive, time consuming, and in many cases the protection system is difficult to acquire in sufficient quantities to perform a decent statistical analysis. Furthermore, a detailed calculation can in many cases provide relevant information about underlying mechanisms that are hard to measure directly.

The report is divided into two parts. In part I, we provide a detailed reference of the physics involved in ballistic impact. In addition, based on fundamental physical principles we rederive and evaluate several analytical models which in principle can be used to describe and predict structural failure in ceramic plates. In the future, we believe the analytical models can form the basis for a new material model of ceramics. In part II, we use the finite element code IMPETUS Afea to evaluate a more detailed numerical model. Both the analytical and numerical model produce crack patterns that are consistent with experiments.

2 Experimental crack patterns

In Fig. 2.1 we show various characteristic crack patterns that can be observed in ballistic experiments. In this case, shots were fired at two targets: a bare alumina tile and an alumina tile with a glass-fiber cover. The images show both the front side, back side, and a cross section of the alumina tile after ballistic impact. From the images we observe the following cracks:

- There are both primary and minor cone cracks propagating through the tile, at an angle relative to the front and back sides. On the front and back sides the cone crack manifests as ring cracks. Note that for lower velocities (175 m/s in the examples shown) the cone crack is not able to completely propagate through the tile.
- Radial cracks appear on both the front and back of the ceramic, and are typically initiated at the point of impact (and directly below on the back side). The radial cracks propagate relatively long distances, and in straight lines that are parallel to the front and back side.
- Directly below the point of impact, and straight through the tile, a median crack appears. The median crack is approximately orthogonal to the tiles back side and front side.
- The horizontal cracks which connect the median cracks to the primary and minor cones are called lateral cracks. The lateral cracks often horizontally split the cone, typically into two (or three) large pieces.
- Directly below the point of impact a so-called plastic zone is formed close to the surface of the tile. In the plastic zone the load is severe and the material exhibits crushing, microcracks, and several other complicated plastic deformation modes.

To be specific, the goal of this report is to understand why these cracking modes appear, review simple mathematical theories which correctly predicts the observed crack patterns, and perform numerical simulations which generate the crack pattern. For additional background information, we refer to the following literature review and related articles [1, 2, 3].

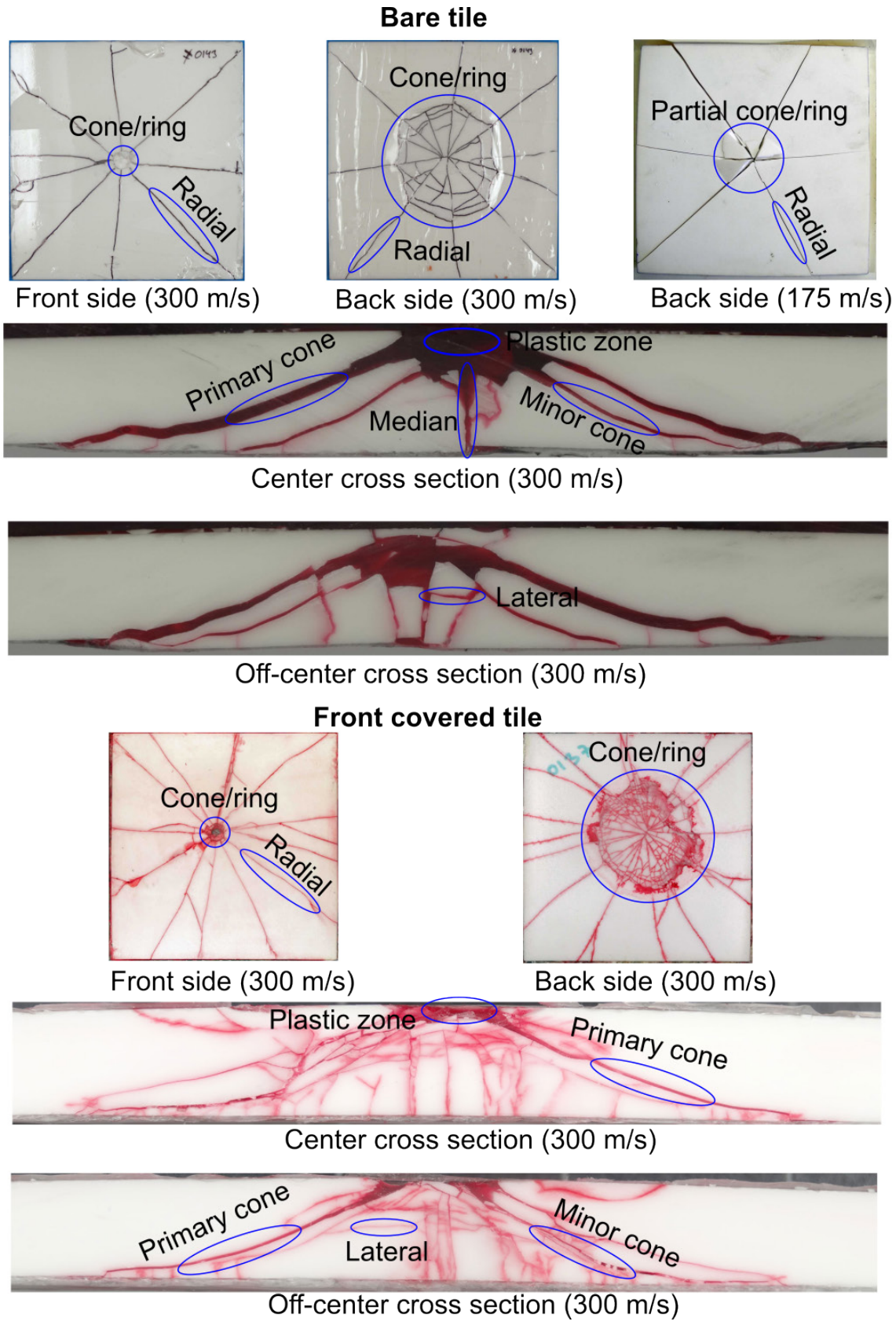

Figure 2.1 An overview of the crack patterns observed in typical experiments. The figure is adapted from [2].

PART I

Overview of analytical models

3 Development of the linear theory

Under standard conditions, ceramics, glass, and concrete are classified as brittle materials. Brittle materials are typically very hard, but are prone to suddenly fail under loading with little deformation. On the other hand, metals, such as steel and aluminum, are classified as ductile materials. A loaded ductile material can be deformed significantly before it breaks, making it possible to shape and form. The differences between the loading history of a brittle and ductile material are summarized graphically in the stress-strain diagrams of Fig. 3.1. The crucial technical point is that, in contrast to ductile materials, the brittle materials exhibit mostly linear behavior and fails while the deformation is still close to being elastic. The linearity enables the use of semi-analytical models to predict failure in ceramics. In broad terms, the dynamic ballistic impact problem is modeled as a quasistatic process and closely follows the theory of Hertzian contact [4]. A review of the application of the Hertzian contact theory to ceramics can be found in [5]. In the civil sciences, a similar linear model is under development for laminated glass; a material which also behaves in a brittle manner [6, 7, 8]. The Hertzian contact theory can be extended by adding plasticity corrections in the far field limit.

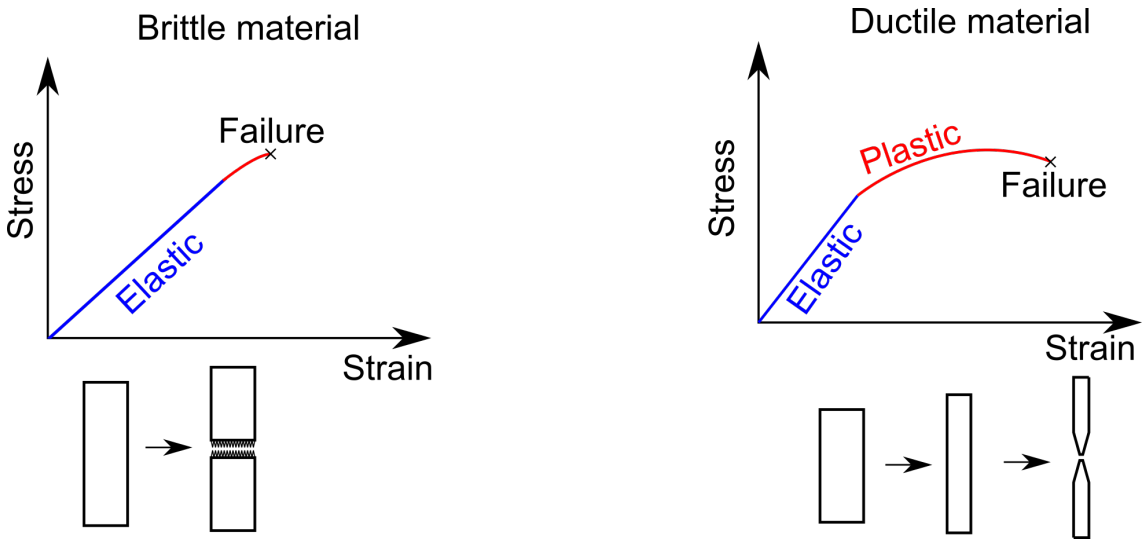

Figure 3.1 A comparison between the general behavior of brittle and ductile materials.

3.1 Hertzian quasistatic contact theory and induced stress

Our discussion is based on Hertz's [4] and Huber's [9] work. Both authors consider the situation where an isotropic elastic sphere of radius R is quasistatically pressed with a force P into an isotropic elastic semi-infinite half space. Due to the rotational symmetry the solution is simplest in a cylindrical coordinate system. We assume that the z-axis is perpendicular to the semi-infinite half space. The geometry is displayed in Fig. 3.2. The complete solution was historically obtained in two steps. First, Hertz obtained the stress and displacement solutions at the surface. Second, Huber extended the solution and determined the induced stresses inside of the semi-infinite half space.

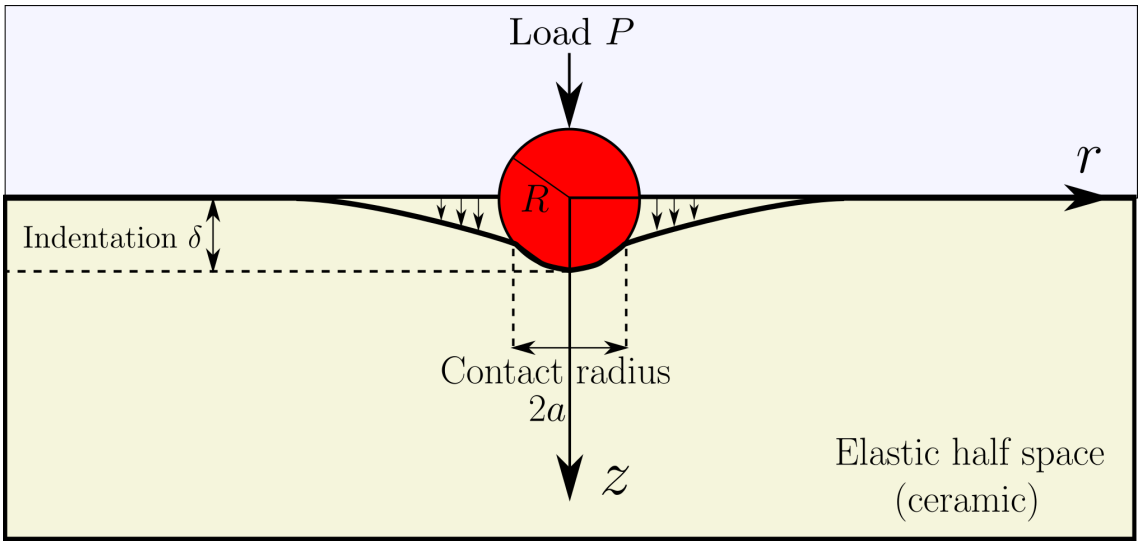

Figure 3.2 Overview over the geometry, where an elastic sphere is pressed into an elastic half space.

3.1.1 Hertz's and Huber's solutions

The process is assumed to be quasistatic so the static equilibrium equations hold,

$$\begin{aligned} 0 &= \frac{1}{r}\frac{\partial}{\partial r}(r\sigma_{rr}) + \frac{1}{r}\frac{\partial \tau_{r\theta}}{\partial \theta} + \frac{\partial \tau_{rz}}{\partial z} - \frac{\sigma_{\theta\theta}}{r}, \\ 0 &= \frac{1}{r}\frac{\partial}{\partial r}(r\tau_{r\theta}) + \frac{1}{r}\frac{\partial \sigma_{\theta\theta}}{\partial \theta} + \frac{\partial \tau_{\theta z}}{\partial z} + \frac{\sigma_{r\theta}}{r}, \\ 0 &= \frac{1}{r}\frac{\partial}{\partial r}(r\tau_{rz}) + \frac{1}{r}\frac{\partial \tau_{\theta z}}{\partial \theta} + \frac{\partial \sigma_{zz}}{\partial z}, \end{aligned} \tag{3.1}$$

where we neglect body forces such as gravity whose only contribution is a small hydrostatic stress. In addition, the following boundary conditions must be satisfied:

1. Infinitely away from the point of contact the displacements are zero.
2. Friction is ignored, so at the surface $z = 0$ the shear stresses are zero.
3. The contact area is circular with an as of yet undetermined radius a. Outside (inside) the contact area the pressure is zero (positive).
4. The surfaces do not penetrate into each other. Instead they deform elastically, giving rise to a corresponding boundary condition.

In the original publication Hertz solves Eq. (3.1) with the appropriate boundary conditions by using analogies from his work on electrostatics. Simply put he introduces two separate potentials which satisfy the Laplace and Poisson equation respectively. These equations are special because in electrostatics their solution is completely specified by the boundary conditions. The difficulty of the problem lies in correctly implementing the 4th boundary condition regarding impenetrability. Hertz overcomes this problem by proposing an ansatz for the contact pressure of the form

$$p = \begin{cases} p_0\sqrt{1-(r/a)^2}, & r < a, \\ 0, & r > a, \end{cases} \tag{3.2}$$

which, by using Hooke's law, turns out to produce the correct contact surface. Here the mean pressure over the contact area is $p_0 = P/\pi a^2$. The system of equations are then solved by standard methods, and we refer to the original articles for the solution procedure.

As mentioned Huber extended the analysis and determined the induced stress distribution throughout the entirety of the semi-infinite half space. The stress-tensor component's explicit form is given in App. A, where we also provide the solution for different indenter geometries. The surface stress distribution obtained by Hertz are obtained by taking the limit $z \to 0$. The displacements follow from Hooke's law. At the contact surface, inside of the circular contact area the stresses are primarily compressive. At the perimeter of the circular contact area the stresses changes sign and becomes tensile. The largest tensile stress occurs on the perimeter of the contact circle and is given by

$$\sigma_{\max} = \frac{1}{2}\,(1 - 2\nu)\,p_0. \tag{3.3}$$

Since the largest tensile stress occurs on the surface at the perimeter of the contact area, this is where we expect the cone crack to show up.

3.1.2 The impenetrability boundary condition

We will briefly comment on the impenetrability boundary condition, as it allows us to determine analytical expressions for the contact radius, indentation, and maximum pressure without diving to deep into the technical details. We consider the situation in Fig. 3.3 where a sphere is pressed into a semi-infinite half space. In the figure, we define the indentation and displacements of the sphere and half space as (δ_1, u_1) and (δ_2, u_2) respectively. The undeformed sphere is described to lowest order by the parabola $r^2/2R$. The impenetrability boundary condition takes the form,

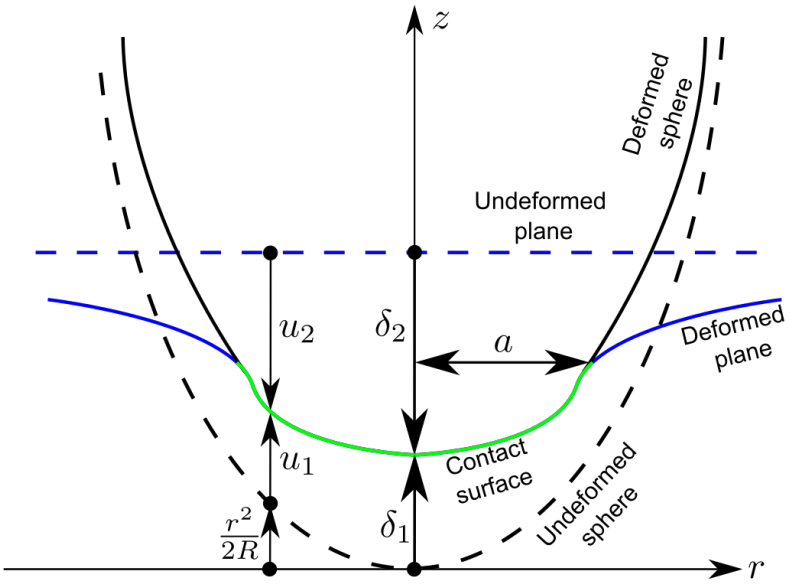

Figure 3.3 The detailed deformation of a sphere and elastic half space when pressed together.

$$\begin{aligned} \delta_1 + \delta_2 &= \frac{r^2}{2R} + u_1(r) + u_2(r), \quad \text{inside the contact area.} \\ \delta_1 + \delta_2 &> \frac{r^2}{2R} + u_1(r) + u_2(r), \quad \text{outside the contact area.} \end{aligned} \tag{3.4}$$

For convenience we define the total indentation as $\delta = \delta_1 + \delta_2$. The contact pressure in Eq. (3.2) produces the displacements

$$u_{1,2} = \frac{1-\nu_{1,2}^2}{E^*}\frac{\pi p_0}{4a}\left(2a^2 - r^2\right), \quad r < a. \tag{3.5}$$

The constant E^* is called the effective elastic contact coefficient and takes the form

$$\frac{1}{E^*} = \frac{1-\nu_1^2}{E_1} + \frac{1-\nu_2^2}{E_2}. \tag{3.6}$$

Here $\{\nu_1, E_1\}$ and $\{\nu_2, E_2\}$ refer to the Poisson ratio and Young modulus of the indenter (sphere) and semi-infinite half space (ceramic) respectively. In addition, the total load becomes

$$P = \int_0^a p(r) 2\pi r \mathrm{d}r = \frac{2}{3} p_0 \pi a^2. \tag{3.7}$$

By inserting Eq. (3.5) into Eq. (3.4) we find the contact radius

$$a = \left(\frac{3PR}{4E^*}\right)^{1/3}, \tag{3.8}$$

and the indentation

$$\delta = \frac{a^2}{R} = \left(\frac{9P^2}{16RE^{*2}}\right)^{1/3}. \tag{3.9}$$

Using Eqs. (3.7) and (3.8) the maximum pressure takes the form

$$p_0 = \frac{3P}{2\pi a^2} = \left(\frac{6PE^{*2}}{\pi^3 R^2}\right)^{1/3}. \tag{3.10}$$

The expressions above are useful because the geometric properties of the problem are given as functions of the external load.

Since both the indenter and half-space are elastic materials one might expect the relationship between the force and indentation to be linear $P \sim \delta$, similar to the restoring force for a harmonic oscillator. Yet, note that Eq. (3.9) can be rewritten to the form $P \sim \delta^{3/2}$, where the exponent represents a deviation from the harmonic oscillator. We can understand this explicitly by modeling the elastic half space as a set of uncoupled springs, all with the same spring constant, see Fig. 3.4. In the literature, this particular discretization is known as Winkler's elastic foundation model [10]. Note that for a spherical indenter each spring is compressed by a different amount, causing a non-uniform contact pressure. If all of the springs where compressed by the same amount the system would be well described by a single harmonic oscillator. Thus it is the non-trivial geometry of the contact surface which causes the peculiar exponent $3/2$.

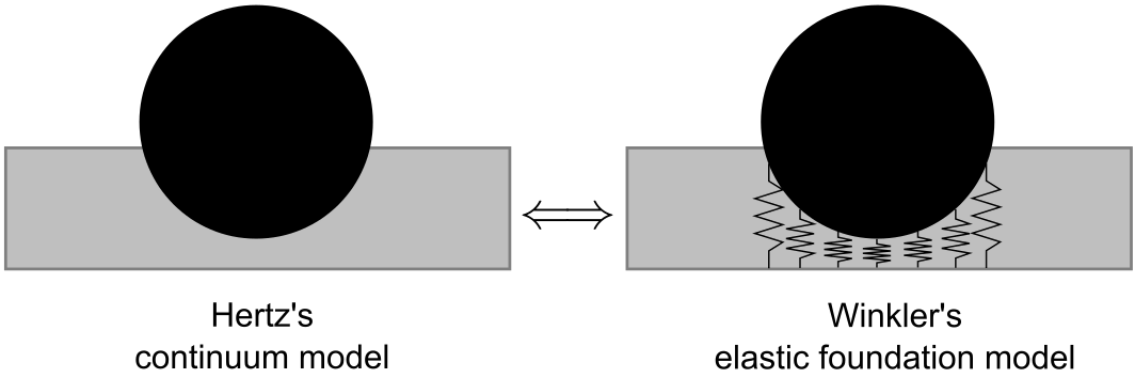

Figure 3.4 A comparison between Hertz's continuum and Winkler's elastic foundation model.

3.1.3 Direction of the cone crack

We will now discuss the relationship between the stress tensor and the direction of the induced cone crack [11]. The direction of the cone crack can be obtained by studying the principal values (eigenvalues) and the corresponding principal directions (eigenvectors),

$$\begin{aligned}
\sigma_1 &= \frac{1}{2}\left((\sigma_{rr}+\sigma_{zz}) + \sqrt{\left[\frac{1}{2}(\sigma_{rr}-\sigma_{zz})\right]^2 + \tau_{rz}^2}\right), \quad V_1 = (\cos\phi^*, 0, \sin\phi^*)\,, \\
\sigma_2 &= \sigma_{\theta\theta}, \qquad\qquad\qquad\qquad\qquad\qquad\qquad\qquad V_2 = (0,1,0)\,, \\
\sigma_3 &= \frac{1}{2}\left((\sigma_{rr}+\sigma_{zz}) - \sqrt{\left[\frac{1}{2}(\sigma_{rr}-\sigma_{zz})\right]^2 + \tau_{rz}^2}\right), \quad V_3 = (-\sin\phi^*, 0, \cos\phi^*)\,.
\end{aligned} \tag{3.11}$$

The angle ϕ^* is given by

$$\tan 2\phi^* = \frac{2\tau_{rz}}{\sigma_{rr}-\sigma_{zz}}. \tag{3.12}$$

The principal values and directions were obtained by diagonalizing the Cauchy stress tensor as shown in App. A.3. Note that σ_1, is always greater than both σ_2 and σ_3, making it the most important contribution to crack formation.

In Fig. 3.5 we have plotted σ_1 as a function of position in a plane through the axis of symmetry. The stress and position are normalized with respect to the mean pressure p_0 and contact radius a respectively. Directly below the region of contact there is a circular region where σ_1 is compressive ($\sigma_1 < 0$). Outside of this region σ_1 is tensile ($\sigma_1 > 0$), and the numerical value decreases with increasing distance from the surface. At the perimeter of the contact surface σ_1 takes its most tensile value $\sigma_1(r = a, z = 0) = \sigma_{\max}$. In the compressive region the material is squashed together and may become crushed, and in the tensile region the material is being torn apart and may begin to crack.

In Fig. 3.5, the dashed lines represent the V_3 directions at each point. Note that the stresses σ_1, σ_2, and σ_3 are distinct and therefore have orthogonal eigenvectors V_1, V_2, and V_3. If σ_1 pulls the material in the $\pm V_1$ direction a crack may begin to form in the V_3 or V_2 direction. Thus as an approximation we conclude that the cracking proceeds orthogonally to V_1. The crack path is therefore determined by the trajectories (V_2 and V_3) of the two other principal stresses. We would expect the cone crack to initiate at the point where σ_1 is the largest, namely at the circle of contact. The crack will simultaneously propagate around the symmetry axis (following the V_2 trajectory) and away (following the V_3 trajectory) from the free surface. The net result is the primary cone crack.

In practice the Hertzian contact theory is accurate, and has withstood the test of time. Historically, the theory was first applied to silicate glass ($\nu = 0.25$) as their transparency makes it easier to measure the cracks with primitive equipment. The theory predicts that the cone crack initiates at the perimeter of the contact circle $r = a$. In practice, the cone crack typically initiates right outside the contact circle, on average in the regime $r = 1.12a$ or $r = 1.19a$. The measured cone angle of $\approx 68.5°$ is also very close to the theoretical value of $\approx 68°$. There are however documented cases where the correspondence is worse [12]. The remaining discrepancies between theory and experiment can typically be explained by the following reasons:

- The theory does not take into account that the cracks modify the stress distribution within the sample.
- The experimental samples may contain inhomogeneity or anisotropies, for example in the form of defects.

- The onset of plasticity in certain regimes introduces new aspects that the elastic contact theory does not take into account.
- An imperfect interface (contact friction, surface defects) may induce additional shear stresses and thereby change the boundary condition.

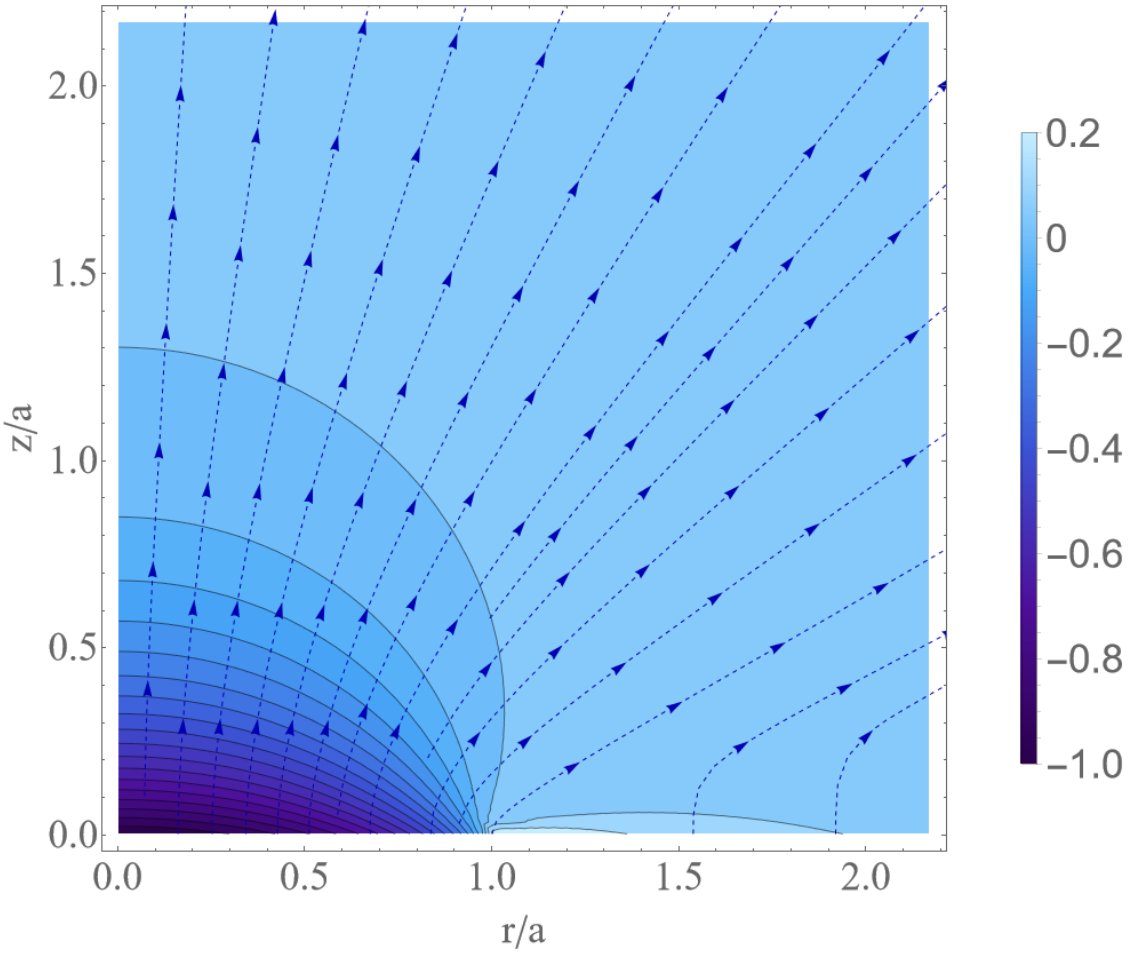

Figure 3.5 Maximum principal stress σ_1 as a function of position in the semi-infinite half space. The dashed lines are the σ_3 trajectories generated by V_3, and they indicate the direction of crack propagation.

3.2 Hertzian dynamic impact theory

We have just considered the quasistatic loading of a ceramic plate. In terminal ballistics the load that the projectile exerts on the ceramic plate is dynamic. The primary difference between the ballistic and quasistatic case is that in the former the load is time dependent, and there are propagating stress (shock)waves. First we present the aspects of the theory, the discussion is based on [13]. Finally, we comment on the assumptions for the theory to be valid.

3.2.1 The quasistatic impact problem

We here consider the elastic regime, where both the sphere and half space is elastic. As derived in Sec. 3.1.2 the relationship between the load P and indentation δ_z is

$$P(t) = \frac{4}{3}E^*\sqrt{R\delta_z^3} \equiv K\delta_z^{3/2}(t), \tag{3.13}$$

where R is the projectile radius, and $1/E^* = (1-\nu_1^2)/E_1 + (1-\nu_2^2)/E_2$. Newton's second law at the contact interface describes the time evolution of the indentation

$$m\frac{\mathrm{d}^2\delta_z}{\mathrm{d}t^2} = -K\delta_z^{3/2}, \tag{3.14}$$

where m is the projectile mass. The second and first integral with respect to δ_z provides the compression-time curve

$$t = \frac{\delta_z^*}{V_z}\int \frac{\mathrm{d}(\delta_z/\delta_z^*)}{\sqrt{1-(\delta_z/\delta_z^*)^{5/2}}}, \tag{3.15}$$

and the maximum compression

$$\delta_z^* = \left(\frac{5mV_z^2}{4K}\right)^{2/5} = \left(\frac{15mV_z^2}{16R^{1/2}E^*}\right)^{2/5}, \tag{3.16}$$

respectively. Here the projectile's impact velocity is given by $V_z = (\mathrm{d}\delta_z/\mathrm{d}t)_{t=0}$. The compression time curve is shown in Fig. 3.6.

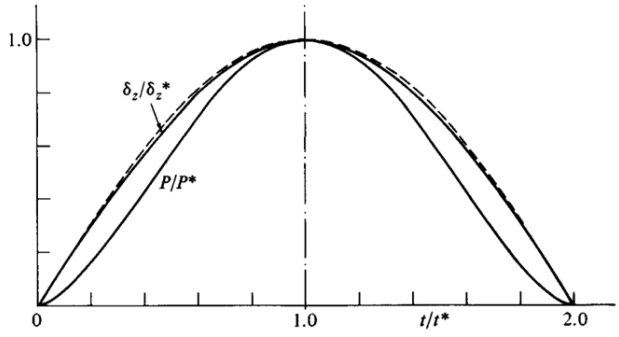

Figure 3.6 Variation of the compression δ_z and force P with time during Hertzian impact. The dashed line represents the function $\sin(\pi t/2t^*)$. *The figure is adapted from [13].*

During the contact, the indentation will first grow to its maximum value as the load increases and then decrease to zero during the unloading phase. Thus from Eq. (3.15) we can obtain the contact time between the sphere and half-space as

$$T_C = 2t^* = 2\frac{\delta_z^*}{V_z}\int_0^1 \frac{\mathrm{d}(\delta_z/\delta_z^*)}{\sqrt{1-(\delta_z/\delta_z^*)^{5/2}}} \approx 2.94\frac{\delta_z^*}{V_z}. \tag{3.17}$$

Here $t^*(=T_C/2)$ is the time at which the load, radius, and indentation take their maximum values.

In the elastic regime the ballistic problem can be modeled as a time dependent load according to Eq. (3.13). The time dependence of the contact radius is given by Eq. (3.8). The time evolution is described by the compression-time curve in Eq. (3.15). At each time step the stress within the half space is given by the corresponding equilibrium Cauchy stress tensor in Eq. (A.8). Note that in the elastic theory the stresses vanish immediately when the load is removed, so the cracking which occurs in the unloading phase is not captured by the theory.

3.2.2 Criteria of validity

The first assumption in the quasistatic theory is that the load changes "slowly". This is necessary so that the system will have time to adjust to equilibrium each time the load changes. The assumption is expected to be valid if the projectile velocity ($\approx 100-850\,\mathrm{m/s}$) is low compared to the speed of sound in the ceramic ($\approx 10000\,\mathrm{m/s}$). Due to the ceramic's high speed of sound this criteria is in practice satisfied.

The second assumption is that we can ignore contributions due to stress wave reflections. The stress wave that initiates at the point of impact will propagate both into the ceramic and also the projectile. Since the ceramic is much heavier than the projectile the pressure wave is often reflected back and forth within both materials many times, before the projectile looses contact with the ceramic. The net effect of many consecutive reflections, is an averaging process such that the stress can be decomposed into a sum of one large average stress field with small perturbations on top. The average stress field is then given by the Hertzian impact theory, and we can neglect the perturbation.

We can make the criteria for ignoring stress waves mathematically more specific. The contact time T_C is given by Eq. (3.17). We introduce the wave time $T_\lambda = L/c_0$, which is the time it takes for a wave to propagate through either the ceramic or sphere. Here $L = 2R$ for the sphere (radius R) and $L = d$ for the ceramic (thickness d). The longitudinal speed of sound is defined as $c_0 = \sqrt{E/\rho}$. The ratio between the wave time and contact time then takes the form

$$\frac{T_\lambda}{T_C} \approx 0.2\frac{L}{R}\left(\frac{V_z}{c_0}\right)^{1/5} \tag{3.18}$$

which should be less than unity for the Hertzian theory to be valid. For impacts in the regime $100-850\,\mathrm{m/s}$ we obtain

$$\begin{aligned} \frac{T_\lambda}{T_C} &\approx \frac{L}{R}(0.07, 0.12) \quad \text{ceramic,} \\ \frac{T_\lambda}{T_C} &\approx \frac{L}{R}(0.09, 0.14) \quad \text{sphere,} \end{aligned} \tag{3.19}$$

so the approximation seems reasonable.

4 Extension to the nonlinear regime

The Hertzian contact theory allows us to understand the formation of cone cracks, yet it does not explain the other types of cracks that occur. An overview of the possible cracks in ballistic experiments were given earlier, see Fig. 2.1. In addition, the elastic theory is unable to describe the unloading phase were the projectile loses contact with the ceramic.

4.1 Yoffe's far-field plasticity theory

The problem of appropriately introducing plasticity into the quasistatic theory has been tackled analytically by Yoffe [14]. The indenter is assumed to have circular contact area of radius a, such that we can exploit axial symmetry. The contact pressure p is assumed to be uniform, such that the loading force is $P = p\pi a^2$. This is an assumption, since we do not know how the contact pressure varies across a plastically deformed contact. Numerical calculations indicate that the assumption is relatively accurate [15]. Nevertheless, the theory certainly captures and describes the underlying mechanisms producing the different types of cracks.

The total stress field obtained by pressing an indenter into a semi-infinite half space is a sum of two contributions, one elastic and one plastic. The primary elastic contribution of the indentation is given by the so-called Boussinesq solution [16], which describes the field produced by a point load P on the flat surface of a semi-infinite half space. The resulting field is long range and proportional to $1/r^2$. Note that the elasticity theory is kept to a very simple[1] analytic form, so that it is easy to use herein. The plastic contribution is more complicated. The plastically deformed zone beneath the indenter has changed shape and volume, but is still attached to the elastic half-space. Mathematically, the plastic region is treated as a singularity which, in the far field, results in a local 'blister'[2] field which decays like $1/r^3$ [17]. The total solution for an indenter which plastically deforms the half-space is

$$
\begin{aligned}
\sigma_{rr} &= \frac{P}{2\pi r^2}\left[1-2\nu-2(2-\nu)\cos\theta\right] + \frac{B}{r^3}4\left[(5-\nu)\cos^2\theta-(2-\nu)\right], \\
\sigma_{\theta\theta} &= \frac{P}{2\pi r^2}\frac{(1-2\nu)\cos^2\theta}{1+\cos\theta} - \frac{B}{r^3}2(1-2\nu)\cos^2\theta, \\
\sigma_{\phi\phi} &= \frac{P}{2\pi r^2}(1-2\nu)\left[\cos\theta-\frac{1}{1+\cos\theta}\right] + \frac{B}{r^3}2(1-2\nu)(2-3\cos^2\theta), \\
\tau_{r\theta} &= \frac{P}{2\pi r^2}(1-2\nu)\frac{\sin\theta\cos\theta}{1+\cos\theta} + \frac{B}{r^3}4(1+\nu)\sin\theta\cos\theta.
\end{aligned}
\tag{4.1}
$$

In the above, we are using spherical coordinates with $r = \sqrt{x^2+y^2+z^2}$, polar angle θ, and azimuthal angle ϕ as shown in Fig. 4.1. The strength B of the blister field is dependent on the maximum applied load, the capability of the half-space to be compacted, and the geometrical shape of the

[1] In principle, we could have used the complete spherical-indenter solution instead of the Boussinesq solution. Alternatively, the Boussinesq field can be viewed as an approximation to the spherical-indenter solution in the far-field limit, $r/a \gg 1$.

[2] In the literature, the word blister comes from the shape of the indentation volume.

impacting projectile. For a material of hardness H [N/m^2], Young modulus E [Pa], and under a load P [N], it follows from dimensional analysis that the strength of the Blister field takes the form

$$B = \text{Dimensionless geometrical factor} \times E \left(\frac{P}{H}\right)^{3/2}. \tag{4.2}$$

The dimensionless geometrical factor depends on the geometry of both the indenter and plastically formed cavity.

We will now demonstrate generally how the Blister field is calculated for an arbitrary indenter. From Yoffe's theory the general relationship between the displaced volume and the blister field is given by

$$Vf = \frac{2\pi B\,(1-2\nu)}{3G} = \frac{4\pi\,(1-2\nu)\,(1+\nu)\,B}{3E}. \tag{4.3}$$

We here used the isotropy relationship $E = 2G(1+\nu)$ between the shear and Young modulus. The densification factor f takes into account processes that do not conserve the volume in the plastic zone. The limiting values $f = 1$ and $f = 0$ represents zero and maximal densification respectively. Next, it is assumed that the displaced volume is equal to the volume of the crater created by the indenter, which we denote as V_i. For a conical, pyramidal (called Vicker), and spherical indenter the crater volume is

$$V_{\text{cone}} = \frac{1}{3}\pi a^3 \cot\alpha, \tag{4.4}$$

$$V_{\text{Vicker}} = \frac{2}{3}\pi a^3 \cot\alpha, \tag{4.5}$$

and

$$V_{\text{Spherical}} = \frac{\pi}{3}R^3\left\{2 - \left[1 - \frac{a^2}{R^2}\right]^{1/2}\left[2 + \frac{a^2}{R^2}\right]\right\} \tag{4.6}$$

respectively. The final relation which is required is the relationship between the hardness, load, and contact area. Generally, this relationship is of the form

$$H = \frac{P}{\alpha_0 a^2}, \tag{4.7}$$

where α_0 is a numerical prefactor which depends on the contact area's shape. For a rectangular area produced by a Vicker indenter $\alpha_0 = 2$. For a circular contact area (e.g. conical indenter or sphere) $\alpha_0 = \pi$. By combining the above three relations we obtain the strength of the Blister field. The simplest expressions are for a cone with angle 68° and a Vicker indenter pressed into glass ($\nu = 0.25$), which takes the forms

$$B_{\text{Cone}} = 0.029 f E \left(\frac{P}{H}\right)^{3/2} \tag{4.8}$$

and

$$B_{\text{Vicker}} = 0.026 f E \left(\frac{P}{H}\right)^{3/2} \tag{4.9}$$

respectively. The expression for a spherical indenter is

$$B_{\text{Sphere}} = \frac{2Ef}{5}\pi R^3\left\{2 - \left(1 - \frac{P}{\pi R^2 H}\right)^{1/2}\left(2 + \frac{P}{\pi R^2 H}\right)\right\}. \tag{4.10}$$

The method outlined here can in principle be used to determine the blister field strength for an indenter of arbitrary shape. Examples for Vicker, conical, and spherical indenters are given in [15, 18, 19, 20]

In Yoffe's model it is assumed that the plasticity is present from the start, without the description of a formation process. Hence, the Blister field does not depend on the yield strength Y. However, by comparing the stresses between Yoffe's model and a cavity expansion model it is found that the models are equivalent if the blister field satisfies the relation

$$B = \frac{2Yc^3}{3}. \tag{4.11}$$

Here c is the plasticity radius. In the cavity expansion model there are three regions of interest: the cavity zone $r < a$, the plastic zone $a < r < c$, and the elastic zone $r > c$. The correspondence between Yoffe's theory and the cavity expansion model is discussed further in [21, 22].

4.2 Cracking mechanisms

We will now discuss how Eq. (4.1) accounts for the various possible cracks. Because there are many possible crack variations, it will be messy and perhaps confusing to plot all the vector fields as we did for the Hertzian contact theory. Instead we will consider the stresses at the surface $\theta = \pi/2$, and along the symmetry axis $\theta = 0$. For convenience, we set $\nu = 1/4$. The plastic zone forms just below the indenter and takes a hemispherical form. The stresses in the half-space are larger for small values of r, so we expect the cracks to initiate close to the plastic zone.

We first consider the stress field in the absence of plasticity, with $B = 0$. The highest tensile stress is $\sigma_{rr}(\theta = \pi/2) = P/4\pi r^2$ and occurs at the surface. The radial surface stress attempts to form surface ring cracks, which develop into a cone crack upon increased loading. The cone formation occurs close to the circle of contact where the radial tensile stress is the largest.

We will now gradually turn on B to a small positive value. The radial surface stress and axial polar stress changes by $\sigma_{rr}(\theta = \pi/2) = P/4\pi r^2 - 7B/r^3$ and $\sigma_{\theta\theta}(\theta = 0) = P/8\pi r^2 - B/r^3$ respectively. The axial polar stress $\sigma_{\theta\theta}$ decays slower with B than the radial surface stress σ_{rr}. At some point the axial polar stress becomes larger than the radial surface stress. When this happens the median crack appears instead of the ring and cone crack.

If B continues to increase the axial polar stress $\sigma_{\theta\theta}(\theta = 0)$ will eventually become so small that the median crack becomes suppressed. Yet, the surface azimuthal stress $\sigma_{\phi\phi}(\theta = \pi/2) = -P/4\pi r^2 + 2B/r^3$ increases and eventually changes sign to become tensile, leading to the onset of radial surface cracks.

When the load is removed $P \to 0$ and B remains constant. The axial radial stress $\sigma_{rr}(\theta = 0) = -3P/2\pi r^2 + 12B/r^3$ becomes tensile upon unloading, and forms a lateral crack below the indentation which is parallel to the surface. During unloading, the axial polar and azimuthal stresses are both compressive. The surface azimuthal stress $\sigma_{\phi\phi}(\theta = \pi/2) = -P/4\pi r^2 + 2B/r^3$ becomes tensile, potentially forming new surface radial cracks. During the unloading phase, there is also a tendency of the existing median crack to propagate towards the surface.

In the above analysis it is clear that there is a connection between the type of crack and component of the stress tensor. To summarize we can draw the following conclusions:

- The surface ring cracks and cone are created by a tensile surface radial stress $\sigma_{rr}(\theta = \pi/2) > 0$
- The surface radial cracks are created by a tensile surface azimuthal stress $\sigma_{\phi\phi}(\theta = \pi/2) > 0$
- The interior median crack is created by a tensile axial polar stress $\sigma_{\theta\theta}(\theta = 0)$

- The interior lateral cracks are created by a tensile axial radial stress $\sigma_{rr}(\theta = 0) > 0$

The relationship between a specific cracking mode and the corresponding stress-tensor component are graphically summarized in Fig. 4.1. All of the cracks occurring in a ballistic experiments, as shown in Fig. 2.1, are captured. Importantly, the analytical theory can also be used to understand how specific cracks can be mitigated by explicitly reducing specific components of the stress tensor through appropriate boundary conditions. For instance the theory predicts that a horizontal confinement pressure should reduce the cone, median, and radial cracks. Similarly, a vertical confinement pressure should reduce the lateral cracking. Improved ballistic protection through confinement has been experimentally verified [23, 24, 25, 26].

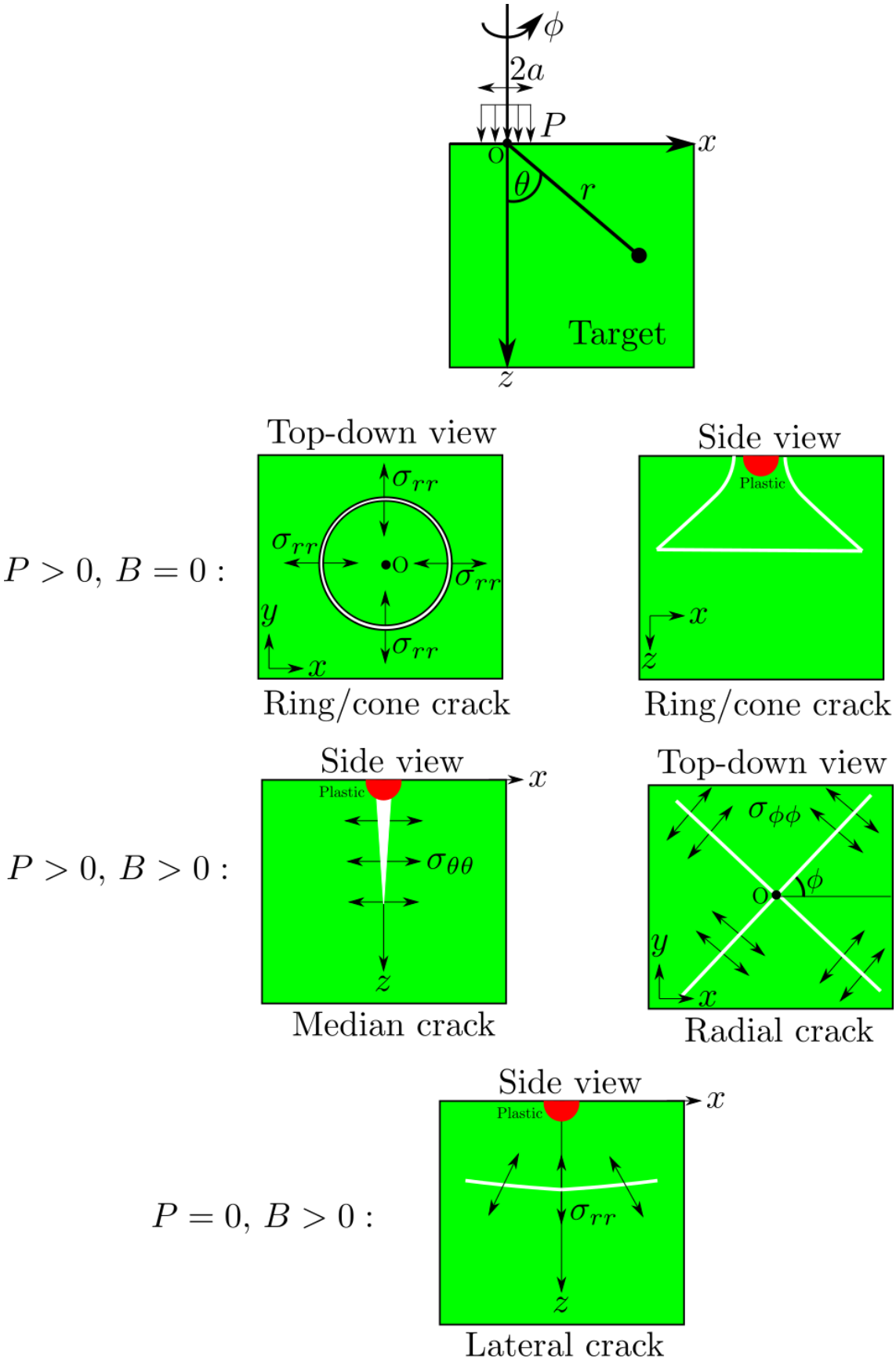

Figure 4.1 An overview of the crack patterns predicted by Yoffe's theory, depending on the load P and degree of plasticity B.

4.3 Application to ballistics

In the quasistatic approximation, the crack growth in a terminal ballistic problem can be viewed in three steps.

1. At the point of impact, there is zero plasticity ($B = 0$) and the load (P) gradually increases. A surface ring crack is produced which gradually develops into a propagating cone crack.
2. Eventually, plasticity occurs so that B increases. For small plasticity, a median crack is formed. With increasing plasticity we expect radial surface cracks to emerge.
3. The unloading phase is characterized by $P \to 0$ and B = constant. We expect the median crack to grow, and potentially new radial cracks to form on the surface.

The above applies to the case where the ceramic thickness is much larger than the projectile length. In reality this is never the case. Instead, at the point of impact, a compressive spherical shockwave that propagates in the ceramic is formed. When the shockwave reaches the opposite side, it is reflected as either a tensile or compressive wave depending on the boundary conditions. Concretely, if the ceramic is without backing a tensile wave is produced leading to additional cracking on the back surface. Since, the shockwave is spherical it seems more likely that the additional cracks will be radial. If the ceramic is backed the reflected shockwave is compressive, and we do expect the cracks to be suppressed. Even without shockwave effects, we emphasize that the theory in its current form has effectively captured all of the experimental cracks in Fig. 2.1.

5 Advantages, limitations, and possible applications

In the previous sections we have reviewed a semi-analytical model to describe when a ceramic will fail during ballistic impact. In this section we summarize the advantages and disadvantages of the model.

The primary advantage of the semi-analytical model is that it is relatively simple to use and run when compared with more technical finite element models. The semi-analytical model is based on sound physical principles, with minimal need for experimental calibration of constitutive material models. We have demonstrated that the Hertzian contact theory gives an explicit expression for the cone crack trajectory, and that the Yoffe plasticity theory can be used to describe secondary cracks such as median, radial, and lateral cracks. Historically, the theoretical trajectory (and angles) of the cone crack has been shown to agree well with the experimental cone crack emerging in transparent silicate glass. In contrast, there are a limited number of experiments on the crack propagation in ceramics in the open literature, presumably because of its role in ballistic protection. Hence, a direct comparison between the analytical model and relevant experiments is hard to perform with confidence.

One disadvantage is that the material strength is independent of the sustained damage, i.e. as the damage increases the material stays just as strong. Strictly speaking, the calculations presented herein is only valid for semi-infinite systems. In real ceramic plates, used in ballistic protection, finite size effects occur because: i) the ceramic is usually thin and ii) the projectile may hit the target close to an edge. In principle, mechanical finite size effects can be incorporated into the model by including appropriate boundary conditions at the edges and surfaces of the plate.

The primary disadvantage of the model is that dynamic effects, particularly the various shock waves, are neglected. In a material subjected to a sudden load three different shock waves emerges as shown in Fig. 5.1: the pressure waves (P-waves), the shear waves (S-waves), and Rayleigh waves (R-waves). The pressure and shear waves are spherical and travels in the bulk of the material,

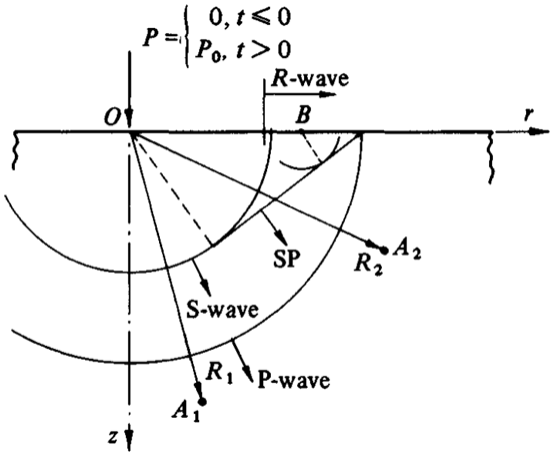

Figure 5.1 Overview over the three types of shock waves emerging in a material subjected to a step-function load. The figure is adapted from [13].

while the Rayleigh waves are circular and propagate on the surface of the material. Consequently, the pressure and shear waves decay like $1/r^2$, and the Rayleigh waves as $1/r$. The situation is further complicated by shock wave reflections from the ceramic edges in a way that depends on the boundary conditions, for instance through the type of backing material. Experience indicates that

the dynamic effects primarily causes a median crack on the backside of the ceramic, while the cone crack is relatively unaffected.

In summary, we have here reviewed an analytical model which is capable of capturing all of the relevant crack patterns, but lack a description of dynamic shockwave effects. We do not expect the shockwave dynamics to significantly change the behavior of the cone crack, but it may affect other minor crack modes. In its current form, the model can be used to predict simplified crack patterns in the regime where dynamic effects are negligible. In the future the analytical model may be expanded into a fully fledged ceramic material model for implementation in finite element codes such as Impetus, LS-Dyna or Abaqus. Alternatively the analytical model can be used in finite element codes as a simplified loading history, which the code will use to predict crack formation and propagation.

PART II

Finite element model

6 Motivation for finite element simulations

In part I we discussed a simple semi-analytical model for crack prediction in thick ceramic plates. The model assumes that the load and response can be described primarily by linear theory with possible extensions to plasticity. In part II we use a finite element approach to describe the cracking of a ceramic plate subjected to impact by a spherical steel projectile. The advantages of the finite element approach compared to the semi-analytical model, is that we are able to incorporate dynamic effects, as well as capturing nonlinear phenomena such as plasticity, and load-dependent material strength. However, the physics can only be described accurately if the materials are being modeled with appropriate material models, and at the same time the associated material parameters are correct. Conversely, there are two things which may go wrong: i) the material model is incorrect (and hence the parameters are irrelevant) and ii) the material model is representative, but the parameters are wrong. In practice, to ensure high quality material models, the finite element approach should be supplemented by several relevant experiments preferably performed at different scales.

Theoretical material models in this work are developed from the experiments in [27]. Concretely, we will model a steel projectile impacting a tile of alumina ceramic. The steel projectile is modeled by the Johnson-Cook model. For the ceramic material model we compare the conventional Johnson-Holmquist-2, to the so-called MMC model. The modeling is performed in the finite element solver "IMPETUS Afea" [28], which we in the following will refer to as Impetus.

Impetus is primarily a Finite Element code, used to describe non-linear mechanical problems where extreme loadings can lead to large deformations. The code was initially developed to model detonation of buried charges under vehicles, but has later grown to include many other uses. Impetus has much in common with Autodyn, but is better suited for certain problems. One of the advantages of Impetus is that it has been explicitly written to run on graphic processing units (GPUs). In many cases GPUs are able to calculate very much faster than central processing units (CPUs). At FFI the calculation part of Impetus is run on a dedicated server with a number of GPUs. This gives considerably larger computing power and speed than Autodyn on a standard PC. Pre- and post processing of the Impetus simulations are done on a standard PC.

7 Screening of material models

The material models are used to describe the behavior of different materials under complex loading conditions. A particularly important notion is that the material model tells us when the material deforms elastically or plastically. Typically, this is encapsulated in a yield criteria which is generally defined as

$$\begin{aligned} \sigma_{\text{Equivalent}} &< \sigma_Y, \quad \text{Elastic deformation,} \\ \sigma_{\text{Equivalent}} &= \sigma_Y, \quad \text{Plastic deformation,} \end{aligned} \tag{7.1}$$

where $\sigma_{\text{Equivalent}}$ and σ_Y are the equivalent stress and material's yield stress respectively. The equivalent stress is a scalar that represents the amount of stress that a material is under, i.e. the complex stress tensor $\boldsymbol{\sigma}$ is mapped to a simple scalar value $\sigma_{\text{Equivalent}}$. The yield stress, marks the transition from elastic to plastic behavior. Concretely, it is the minimum stress at which a solid will undergo permanent deformation or plastic flow without a significant increase in the load or external force. The yield stress depends on the loading, but also on how damaged, stretched, or strained the material has become during the loading process. A fundamental assumption of continuum mechanics is that the equivalent stress can not be larger than the yield stress. Depending on the model, during plastic deformation, the yield stress may increase or stay constant as the loading increases. In any case, the equality $\sigma_{\text{Equivalent}} = \sigma_Y$ is always preserved in the plastic regime.

7.1 Von Mises yield criteria

One particular choice of equivalent stress is the von Mises stress, which we denote as σ_V. Concretely, the von Mises stress $\sigma_V = \sqrt{3J_2}$ is defined in terms of the second invariant of deviatoric stress $J_2 = \frac{1}{2}\boldsymbol{s} : \boldsymbol{s}$, where $\boldsymbol{s}$ is the deviatoric stress tensor.

The equation $\sigma_V = \sigma_Y$ defines the so-called material yield surface which, for the von Mises case, takes the shape of a cylinder in the principal stress coordinate system $(\sigma_1, \sigma_2, \sigma_3)$. The radius of the cylinder is $\sqrt{\frac{2}{3}}\sigma_Y$. Note that geometrically, since the Yield strength usually varies with e.g. strain, the radius of the yield surface changes during loading. In finite element codes, the dynamic behavior of the yield strength σ_Y is typically controlled by constitutive relations. Two constitutive relations that are relevant for this work are the Johnson-Cook model and Johnson-Holmquist model.

7.2 The Johnson-Cook model

In a general finite element description, the Johnson-Cook [29, 30] (JC) model is perhaps the most common approach to describe the deformation of metals. In the context of terminal ballistics, the metallic parts of the projectile and target is governed by the JC model. The three key material responses, encapsulated by the JC model, are strain hardening, strain rate hardening, and thermal softening. These three ingredients are combined in a multiplicative manner which gives rise to the explicit form of the JC constitutive model

$$\sigma_Y = \underbrace{\left[A + B\left(\epsilon^p_{\text{eff}}\right)^N\right]}_{\text{Strain hardening}} \underbrace{\left[1 + C\ln\dot{\epsilon}\right]}_{\text{Strain rate hardening}} \underbrace{\left[1 - (T_H)^M\right]}_{\text{Thermal softening}}. \tag{7.2}$$

Here the physical variables are the von Mises yield stress σ_Y, the effective plastic strain ϵ^p_{eff}, the effective plastic strain rate $\dot{\epsilon} = \dot{\epsilon}^p_{\text{eff}}/\dot{\epsilon}_0$, and the homologous temperature $T_H = (T - T_R)/(T_M - T_R)$. Furthermore, $\dot{\epsilon}_0$ and T_R are the reference strain rate and temperature. The local and melting temperature is denoted by T and T_M respectively.

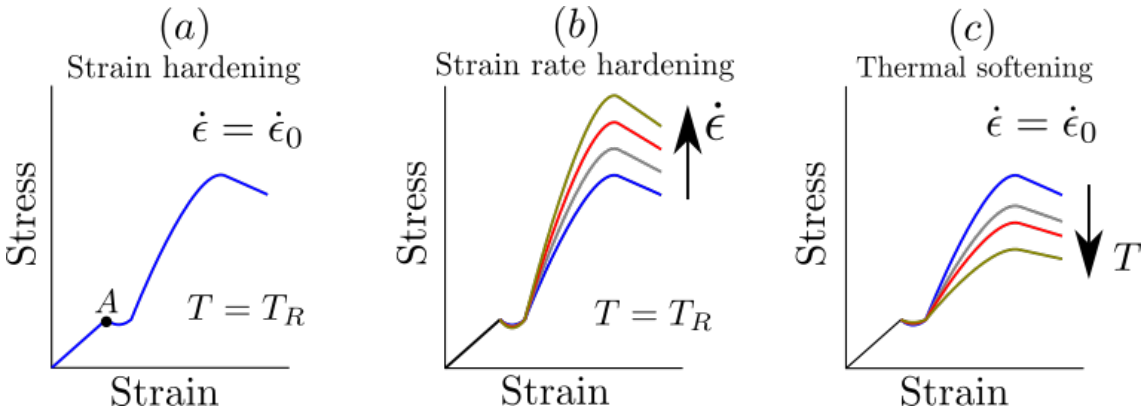

Figure 7.1 An illustration of (a) *strain hardening,* (b) *strain rate hardening, and* (c) *thermal softening.*

To get a better understanding of the behavior of the JC model it is useful to consider how the the numerical parameters $\{A, B, N\}$, $\{C\}$, and $\{M\}$ are obtained from experiments. We will assume that we have performed measurements to obtain three sets of curves as in Fig. 7.1.

To determine $\{A, B, N\}$ we use a single stress-strain curve as shown in Fig. 7.1 (a). The test was performed at some fixed temperature and strain rate which we choose to be our reference variables T_R and ϵ_0. The stress at which the material ceases to behave elastically is the yield stress A. If we express the JC model as

$$\ln(\sigma_Y - A) = N \ln \epsilon + \ln B \tag{7.3}$$

and plot the left hand side (LHS) as a function of logarithmic strain $\ln \epsilon$, then N and B is found from the the slope and intercept of the straight-line best fit.

To determine C we consider a family of stress-strain curves whose individuals all have the same temperature $T = T_R$ but different strain rates as shown in Fig. 7.1. (b). We then express the JC model as

$$\frac{\sigma}{A + B\left(\epsilon^p_{\text{eff}}\right)^N} = 1 + C \ln \dot{\epsilon} \tag{7.4}$$

and plot the LHS as a function of logarithmic strain rate $\ln \dot{\epsilon}$. The parameter C is then determined from the straight-line best fit whose intercept is 1.

To determine M we consider a family of stress-strain curves whose individuals all have the same strain rate $\dot{\epsilon} = \dot{\epsilon}_0$ but different temperatures as shown in Fig. 7.1. (c). By expressing the JC model as

$$\ln\left(1 - \frac{\sigma_Y}{A + B\left(\epsilon^p_{\text{eff}}\right)^N}\right) = M \ln T \tag{7.5}$$

and plotting the LHS as a function of the logarithmic temperature $\ln T$, the parameter M is given as the slope of the straight-line best fit which passes through the origin.

The JC model is considered the go-to description for the deformation of metals during high strain rates. Yet there are at least three limitations. Firstly, the JC model can not describe the necking mechanism, where the stress decreases with increasing strain. Secondly, since the hardening and softening effects are included in a multiplicative law the effects are independent and not coupled to each other. Thirdly, the model is isotropic and can therefore not take into account directional dependence.

As the metal deforms plastically, it gradually becomes more and more damaged. The damage accumulation is described by

$$\dot{D} = \frac{\dot{\epsilon}^p_{\text{eff}}}{\epsilon_f}, \tag{7.6}$$

where the plastic strain required to fracture is given by

$$\epsilon_f = \underbrace{\left[D_1 + D_2 \exp D_3 \left(\frac{\sigma_m}{\sigma_V}\right)\right]}_{\text{Tension softening}} \underbrace{[1 + D_4 \ln \dot{\epsilon}]}_{\text{Strain rate hardening}} \underbrace{[1 + D_5 T_H]}_{\text{Thermal softening}} . \tag{7.7}$$

The expression in the first bracket says that the fracture strain decreases as the hydrostatic tension σ_m increases. The expressions in the second and third bracket represent the effects of strain rate and temperature respectively.

7.3 Ceramic Johnson-Holmquist 2 model

In the literature, when modeling ceramic behavior under ballistic impact the standard solution is to use the Johnson-Holmquist 2 (JH2) model[3]. The JH2 model is a so-called soft plasticity model, which means that as the material is loaded it eventually becomes damaged and gradually goes from an intact to a completely damaged state. The yield function for the JH2 model has the form

$$f(\boldsymbol{\sigma}, D) = \sigma_V(\boldsymbol{\sigma}) - \sigma_Y(\boldsymbol{\sigma}, D) \tag{7.8}$$

where σ_V is the von Mises equivalent stress, σ_Y is the yield stress, and D is a scalar that represents the amount of damage. In the JH2 model the current yield stress is given as an interpolation between the intact and completely damaged yield strength curve,

$$\sigma^*_Y(\boldsymbol{\sigma}, D) = (1 - D)\sigma^*_i(\boldsymbol{\sigma}) + D\sigma^*_f(\boldsymbol{\sigma}). \tag{7.9}$$

The asterisk $(*)$ indicates that the values are normalized with respect to the equivalent stress at the Hugoinot elastic limit. Note that when $D = 0$ and $D = 1$ the ceramic is completely intact and completely damaged respectively.

The yield strength of an intact and completely damaged (fractured) ceramic can be expressed as

$$\begin{aligned} \sigma^*_i(\boldsymbol{\sigma}) &= A \left(\frac{T + p(\boldsymbol{\sigma})}{P_{\text{HEL}}}\right)^n (1 + C \ln \dot{\epsilon}) , \\ \sigma^*_f(\boldsymbol{\sigma}) &= B \left(\frac{p(\boldsymbol{\sigma})}{P_{\text{HEL}}}\right)^m (1 + C \ln \dot{\epsilon}) . \end{aligned} \tag{7.10}$$

[3]The "2" represents that the original Johnson-Holmquist model was modified. The modification was necessary because the transition from an intact to a damaged material was originally treated as discontinuous.

Here A, B, n, m, T and P_{HEL} are material properties and $\dot{\epsilon}$ is the rate of equivalent plastic strain normalized with respect to the reference rate $\dot{\epsilon}_0$.

The accumulation of damage in the JH2 model is very similar to the JC model. The difference is that the plastic strain required to fracture is given by

$$\epsilon_f = D_1 \left(p^* + T^*\right)^{D_2} \tag{7.11}$$

in the JH2 model. Here D_1 and D_2 are the damage parameters.

The material pressure is defined through the trace of the stress tensor $p = -\sigma_{ii}/3$, and it obeys a polynomial equation of state on the form

$$p = \begin{cases} K_1\mu + K_2\mu^2 + K_3\mu^3 + \Delta p & \text{Compression,} \\ K_1\mu & \text{Tension.} \end{cases} \tag{7.12}$$

The equation of state is independent of the damage model. Here $\mu = \rho/\rho_0 - 1$ is the change in density during a deformation. The term Δp is known as the bulking pressure, and increases as the material gradually becomes damaged.

The greatest weakness of the JH2 model (and ceramic models in general) is that it contains a lot of parameters, where only some are measurable. The remaining parameters must be inferred, by assuming the mathematical model to be true. This has led to that in the literature there are several different parameter choices for the same material. We have extensively analyzed the literature, and provide examples of the parameter values for alumina in Tab. 7.1. It is beyond the scope of this project to determine these parameters from experiment. Therefore we have in the following relied on parameter choices used in the literature. Arguably the most important reference is the implementation of the JH2 model in LS-Dyna [31], because it typically serves as a baseline for parameter choices in other references. For completeness we also include the LS-Dyna parameter choices for other ceramics than alumina in Tab. 7.2. We emphasize that the uncertainty in parameter choices makes it possible to tune parameters to better fit a particular set of experimental data, which leads to loss of generality. In this report we will not attempt parameter tuning, but instead extract universal features and attempt to qualitatively understand the underlying physics which after all has the most value in designing new armor systems.

Table 7.1 JH2 parameters for alumina reported by different references.

Parameter	Symbol	Unit	LS-Dyna [31]	Toussaint [27]	Westerling [32]	Tasdemirci [33]	Ning [34]	Lundberg [35]
Density	ρ	kg/m^3	3700	3860	3800	3890	3625	3800
Shear modulus	G	GPa	90.16	90.16	135	152	109.7	135
Strength Constants								
Yield surface parameter	A	-	0.93	2.139	0.989	0.88	0.88	0.989
Failure surface parameter	B	-	0.31	0.31	0.70	0.45	0.28	0.77
Strain rate parameter	C	-	0.00	0.00	0.0	0.007	0.007	0.0
Fracture strength exponent	m	-	0.6	0.6	1.0	0.6	0.60	1.0
Intact strength exponent	n	-	0.6	0.6	0.3755	0.64	0.64	0.3755
Reference strain rate	$\dot{\epsilon}_0$	$1/s$	1.00	1.00	1.0	1	1	1
Tensile strength	T	GPa	0.2	0.2	0.127	0.462	0.262	0.13
Hugoinot elastic limit	HEL	GPa	2.79	2.79	8.3	7.00	5.3	9.3
Damage Constants								
Failure strain parameter	D_1	-	0.005	0.0025	0.01	0.0125	0.02	0.01
Failure strain parameter	D_2	-	1.00	0.5	1.0	0.70	0.83	1.0
Equation of State								
Bulk modulus	K_1	GPa	130.95	130.95	200	231	228.6	200
Quadratic bulk stiffness	K_2	GPa	0.00	0.00	0.0	-160	191.4	0.0
Cubic bulk stiffness	K_3	GPa	0.00	0.00	0.0	2774	111.5	0.0
Bulking parameter	β	-	1.00	1	1	1	1	1

Table 7.2 The JH2 parameters for various ceramics as implemented in LS-Dyna [31]

Parameter	Symbol	Unit	B_4C	SiC	AlN	Al_2O_3	Silica Float Glass
Density	ρ	kg/m^3	2510	3163	3226	3700	2530
Shear modulus	G	GPa	197	183	127	90.16	30.4
Strength Constants							
Yield surface parameter	A	-	0.927	0.96	0.85	0.93	0.93
Failure surface parameter	B	-	0.7	0.35	0.31	0.31	0.088
Strain rate parameter	C	-	0.005	0.00	0.013	0.0	0.003
Fracture strength exponent	m	-	0.85	1	0.21	0.6	0.35
Intact strength exponent	n	-	0.67	0.65	0.29	0.6	0.77
Reference strain rate	$\dot{\epsilon}_0$	1/s	1.00	1.00	1.0	1	1
Tensile strength	T	GPa	0.26	0.37	0.32	0.2	0.15
Hugoinot elastic limit	HEL	GPa	19	14.567	9	2.79	5.95
Damage Constants							
Failure strain parameter	D_1	-	0.001	0.48	0.02	0.005	0.053
Failure strain parameter	D_2	-	0.5	0.48	1.85	1.0	0.85
Equation of State							
Bulk modulus	K_1	GPa	233	204.785	201	130.95	45.4
Quadratic bulk stiffness	K_2	GPa	-593	0	260	0	-138
Cubic bulk stiffness	K_3	GPa	2800	0.00	0.0	0	290
Bulking parameter	β	-	1.00	1	1	1	1

7.4 Preliminary JH2 simulations

In the following we present simulations of spherical projectile impact upon ceramic tiles. The simulation setup is inspired by the experimental data provided in [27]. A spherical steel projectile with velocity 300 m/s and diameter $D = 6.35$ mm, impacts a stationary $101.6\,\text{mm} \times 101.6\,\text{mm} \times 13\,\text{mm}$ alumina tile. Both the projectile and alumina tile is discretized by quadratic hexahedral elements. The projectile is modeled by a simple Johnson-Cook model with parameters as shown in Tab. 7.3. In the simulations, we have kept the projectile parameters constant, and varied the ceramic parameters. We have utilized quarter symmetry, i.e. only a quarter of the projectile and ceramic is modeled. The mesh is refined (level 3) around the point of impact in a cylindrical region with radius $5D$.

Table 7.3 The Johnson-Cook parameters for the spherical projectile.

Parameter	Symbol	Unit	Value
Density	ρ	kg/m^3	7800
Young's modulus	E	GPa	210
Poisson's ratio	ν	-	0.3
Initial yield strength	A	GPa	2.4824
Hardening parameter	B	GPa	1.4985
Hardening exponent	n	-	0.19
Strain rate hardening	C	-	0.027
Thermal softening exponent	M	-	0.66
Reference temperature	T_R	K	293.15
Melting temperature	T_M	K	1760.15
Heat capacity	C_p	$\frac{\text{J}}{\text{kg K}}$	476.97501
Linear Hugoinot slope coefficient	S	-	1.578
Gruneisen gamma	Γ	-	1.60

As pointed out in Sec. 7.3, there is large uncertainty in the literature parameter choices when using the JH2 model to simulate alumina. One might expect that the aforementioned parameter uncertainty arises because the results are relatively independent of a subset of the corresponding parameters. In the following, we demonstrate that the ceramic behavior is very sensitive on the choice of JH2 parameters. Our findings explicitly points out that the parameter uncertainty is a significant unresolved issue when modeling ceramics with the JH2 model. In Fig. 7.2 we have plotted simulations with the JH2 parameter choices shown in Tab. 7.1. Based on the experiment we expect to see a clear cone fracture and a couple of radial cracks. Only three (Toussaint, Westerling, Lundberg) out of six simulations somewhat captures the cone fracture. The radial cracks may become more distinct by decreasing the element size. In the remaining three (LS-Dyna, Tasdemirci, Ning) the cone fracture is absent, and the ceramic appears to be too easily shattered. The absence of the cone might be explained by considering that the corresponding JH2 parameters has been adapted to experiments which only focus on the penetration process, without including a description of crack formation. All six simulations share a common issue, namely that the elements eventually become very inverted. This occurs because when an element becomes completely damaged ($D = 1$) the material model dictates that the element looses its resistance to deformation for negative pressures, but not for positive pressures. It is possible to partially mask this behavior by introducing geometric

erosion criteria, but not in a systematic way. The issues pointed out here, in addition to those pointed out in [2], indicates that it is difficult to tune the JH2 parameters to obtain experimentally consistent simulations. Therefore we will in the following investigate the new material model (MMC), which has been developed by the Impetus team as an alternative to the JH2 model.

7.5 The Impetus MMC model

Due to the aforementioned issues with the JH-2 model, the Impetus team has developed an alternative which is referred to as the MMC model. In this section we provide an overview of how the MMC model works. Similar to the JH-2 model, the material strength σ_Y is described as a function of pressure by an intact and failed curve.

The intact failure strength is defined by two known points and a cap, a total of four input parameters, as shown in Fig. 7.3. The point $(\sigma_c/3, \sigma_c)$ corresponds to an uniaxial compression test and (P_x, σ_x) is an arbitrary point on the yield strength curve. Explicitly the yield strength is defined as

$$\sigma_Y = \begin{cases} c_1 P + c_2, & P < P_t, \\ \sigma_{\text{cap}} \left(1 - e^{-c_3 P + c_4}\right), & P > P_t, \end{cases} \tag{7.13}$$

where the transition point is given by $P_t = \max\{\sigma_c, P_x\}$. The parameters c_1, c_2, c_3, and c_4 are calculated in the solver based on the input $\{\sigma_c, \sigma_x, P_x, \sigma_{\text{cap}}\}$, and are chosen to ensure continuity at the transition point.

The failed material strength are specified by two parameters α and ϵ_{fail}. The first is known as the failed-to-intact material strength ratio and is defined as $\alpha = \sigma_{Y,\text{Failed}}/\sigma_{Y,\text{Intact}}$. Note that if $\alpha = 0$ the material is completely broken, and if $\alpha = 1$ the material is indestructable. In addition to the reduction according to α, the failed material strength is shifted so that it passes through the origin such that the hydrostatic tensile strength of the failed material is zero. Similar to the JH-2 model the current material strength is given as a damage-dependent interpolation between the intact and failed material strength. The damage parameter is given as $D = \min\{1.0, \epsilon_p/\epsilon_{\text{fail}}\}$. So the amount of plastic strain ϵ_p determines the damage of the material, where the element can maximally sustain a plastic strain of ϵ_{fail}. Note that if $\epsilon_{\text{fail}} = 0$, the element becomes completely damaged as soon as plastic strain occurs which is a relevant limit for a brittle material such as ceramics.

There are three possible yield criteria, von Mises (Yield = 0), Rankine (Yield = 1), or an interpolation (Yield $\in (0, 1)$) between the two. Here "Yield" refers to a specific Impetus parameter. We utilize the von Mises criteria, as we do not want to overcomplicate an already complicated system.

The MMC model is also able to describe bulking, where a damaged material expands in volume and typically the pressure increases with plastic flow. The maximum bulking strain is set by the cap on volumetric strain $\epsilon_{v,\max}$. A parameter β controls the direction of plastic flow. For $\beta = 0$ the pressure is constant with plastic flow, and for $\beta = 1$ the pressure increases with plastic flow. Bulking is described by $\beta > 0$ and $\epsilon_{v,\max} > 0$.

To describe strain rate dependency the yield strength is scaled up by a factor

$$\text{rfac} = (1 + \dot{\epsilon}/\dot{\epsilon}_0)^C . \tag{7.14}$$

Here $\dot{\epsilon}_0$ is the reference strain rate, and C is the strain rate exponent. The hydrostatic tensile strength is scaled by an additional parameter ψ.

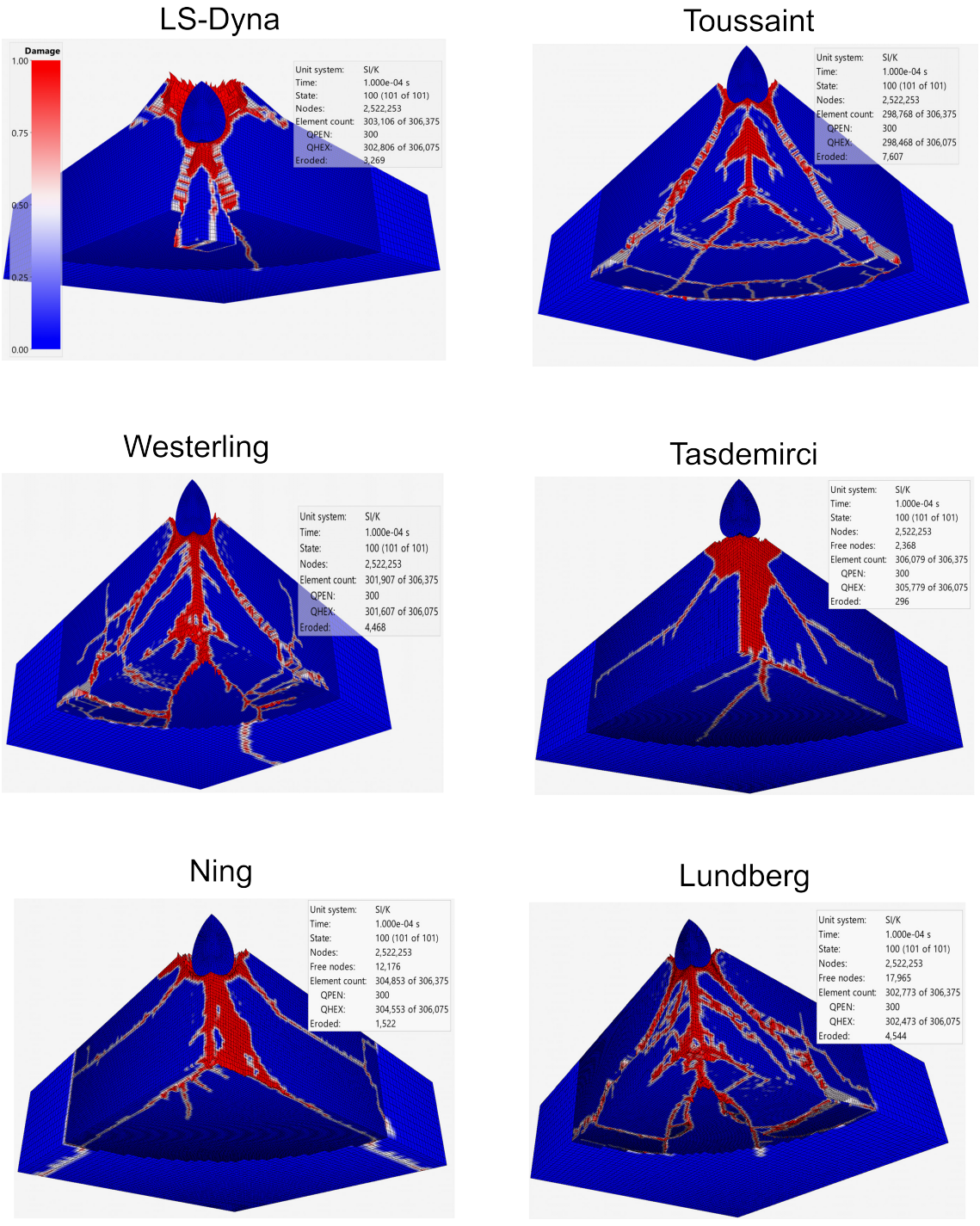

Figure 7.2 *Crack formation as a function the various JH2 parameters in Tab. 7.2. The simulations show a spherical projectile (300 m/s) impacting a 101.6 mm × 101.6 mm × 13 mm alumina plate. We have used quarter symmetry and a cylindrical mesh-refinement region.*

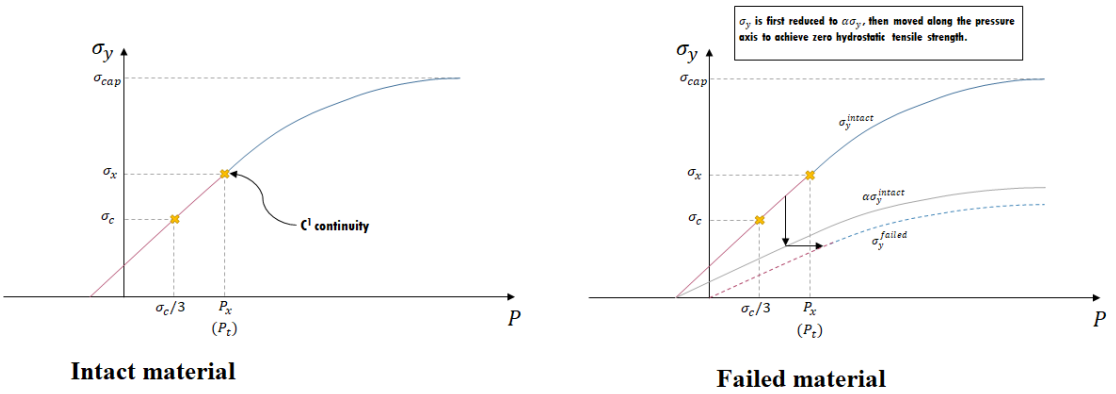

Figure 7.3 The yield strength as a function of pressure for an intact and damaged ceramic, in the MMC model.

The damping is modeled through a viscous stress σ_v which is added to the elastic stress. The viscous stress is proportional to the strain rate $\dot{\epsilon}$. The strength of the damping is controlled by the parameter d [Pa s], and the time the damping is active is controlled by the parameter d_{dec} [s]. For $d_{\text{dec}} > 0$ the strain rate at time t contributes to the viscous stress at $t + d_{\text{dec}}$. For $d_{\text{dec}} = 0$ the viscous stress depends only on the instantaneous strain rate. Mathematically, the damping is implemented as

$$\sigma_v = \begin{cases} \frac{d}{d_{\text{dec}}} \int_0^t \dot{\epsilon}(\tau) e^{\frac{t-\tau}{d_{\text{dec}}}} \mathrm{d}\tau & d_{\text{dec}} > 0, \\ \sigma_v = d \cdot \dot{\epsilon}(t) & d_{\text{dec}} = 0. \end{cases} \tag{7.15}$$

In Impetus, the default parameters of the MMC model is calibrated for silicon carbide. The ceramic of relevance here is alumina. The appropriate parameter values for alumina was extracted from the experiments performed by Toussaint [27]. Specifically the parameters ρ, $G = E/(2\,(1+\nu))$, σ_x, and p_x were updated based on Tab. 1 in Toussaint's article. The MMC model takes a single value of shear stress as input instead of the Young's modulus and the Poisson ratio. For σ_c and σ_x we used the measured uniaxial yield strength and uniaxial tensile strength respectively. The complete alumina model is given in Tab. 7.4.

Table 7.4 The MMC parameters for the alumina ceramic, inspired by [27].

Parameter	Symbol	Unit	Value
Density	ρ	$\mathrm{kg/m^3}$	3860
Shear modulus	G	GPa	147.6
Uniaxial compressive strength	σ_c	GPa	5.75
Arbitrary stress point	σ_x	GPa	0.26
Arbitrary pressure point	P_x	GPa	0.09
Stress cap	σ_{cap}	GPa	15
Failed-to-intact ratio	α	-	0.6
Maximum plastic strain	ϵ_{fail}	-	0
Type of yield surface	-	-	0 (Mises)
Bulk modulus	K	GPa	234.6
Bulking parameter	β	-	0.0
Cap on volumetric strain of bulking	$\epsilon_{v,\mathrm{max}}$	-	0
Strain rate parameter	C	-	0.03
Reference strain rate	$\dot{\epsilon}_0$	$1/\mathrm{s}$	0.01
Rate dependency of hydrostatic tensile strength	ψ	-	0
Damping strength	d	Pa s	100
Damping decay coefficient	d_{dec}	s	0

8 Ballistic loading and crack formation in an MMC ceramic

We will here show the results of a preliminary simulation using the MMC model, using the parameters from Tab. 7.4. The Impetus file can be found in App. B.2. Except for that the ceramic is now modeled using the MMC model, the simulation setup is exactly the same as in Sec. 7.4. For convenience we re-state the simulation details here:

- Spherical projectile with impact velocity 300 m/s and diameter $D = 6.35$ mm, described by the Johnson-Cook model in Tab. 7.3.
- The alumina tile has dimensions 101.6 mm × 101.6 mm × 13 mm and is described by the MMC model with parameters from Tab. 7.4.
- Both the projectile and alumina are discretized by quadratic hexahedral elements.
- Utilized quarter symmetry, and the mesh is refined (level 3) around the point of impact in a cylindrical region with radius $5D$.

In Fig. 8.1 we plot the damage evolution of the ceramic. Each subfigure also shows the projectile velocity as a function of time. The order of crack initiation is as follows:

1. The cone crack initiates almost immediately after impact, see Fig. 8.1a.
2. Upon impact a compressive wave traverses the ceramic. At the backside the compressive wave is reflected as a tensile wave, due to the free boundary condition. Consequently, a localized plastic zone is created at the backside, directly below the point of impact, see Fig. 8.1b. From the localized plastic zone radial and median cracks are initiated, see Fig. 8.1c.
3. During the unloading phase, where the projectiles velocity changes sign, lateral cracks (parallel to the top surface) are initiated from the central median crack, see Figs. 8.1e, 8.1f, 8.1g, and 8.1h.
4. The cone crack has propagated throughout the thickness of the ceramic, and a ring crack on the backside becomes visible. At $t = 38.5\,\mu$s new radial cracks are initiated on the top surface (not shown in Fig). The radial cracks, which initiated on the back side, have grown all the way around to the frontside. These features can be seen in Figs. 8.1i and 8.1j.

The order of the crack initiation during the ballistic impact in Fig. 8.1, is remarkably similar to the crack initiation predicted by the Yoffe plasticity theory in Fig. 4.1. The only difference is that we did not observe radial cracks on the front surface during the loading phase, but that might change as the impact velocity is increased.

In Fig. 8.2 we directly compare the JH2 model, the MMC model, and experimental results. The preliminary simulation suggests that the MMC model outperforms the JH2 model in several ways. Not only does the crack pattern seem to more closely match the experiments, the MMC elements does not suffer from distortion as was the case for the JH2 model. Based on these observations, we choose to proceed with studying the MMC model.

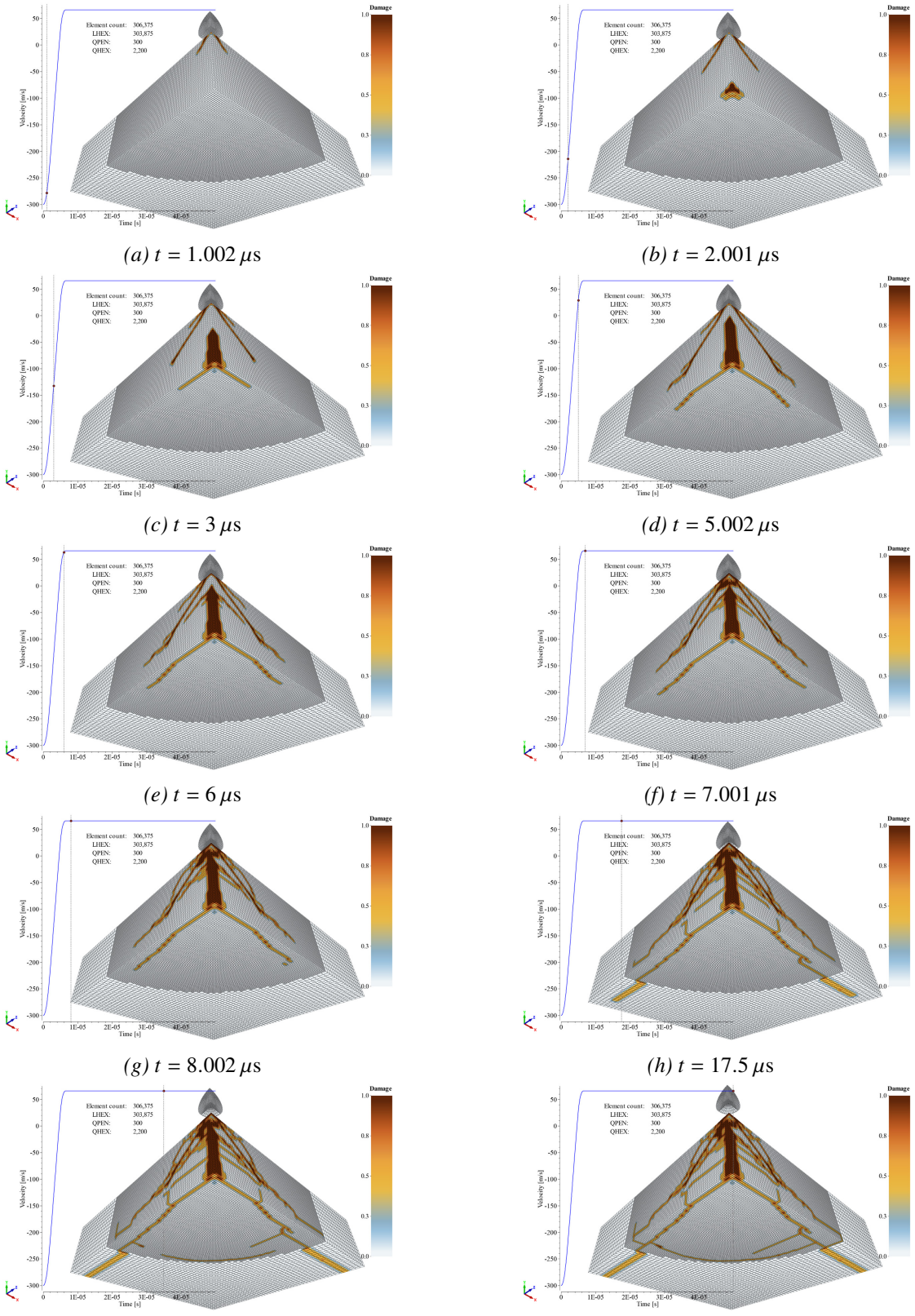

(a) $t = 1.002\,\mu s$ (b) $t = 2.001\,\mu s$

(c) $t = 3\,\mu s$ (d) $t = 5.002\,\mu s$

(e) $t = 6\,\mu s$ (f) $t = 7.001\,\mu s$

(g) $t = 8.002\,\mu s$ (h) $t = 17.5\,\mu s$

(i) $t = 35\,\mu s$ (j) $t = 50\,\mu s$

Figure 8.1 The crack development in the MMC ceramic as a function of time.

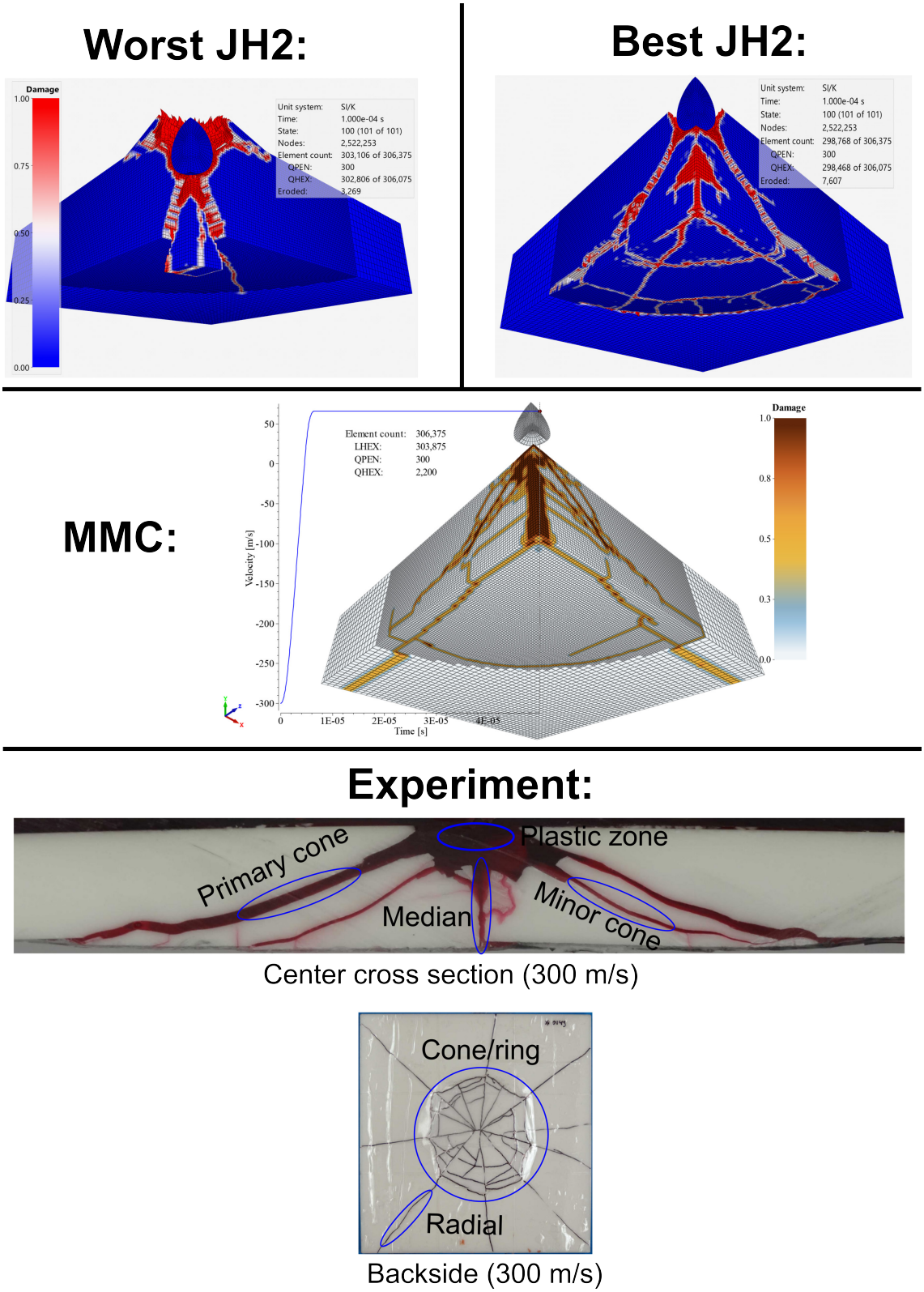

Figure 8.2 A comparison between the JH2 model, the MMC model, and experimental results.

8.1 Damage vs velocity

In the following we will vary the projectile velocity from $10 - 800\,\mathrm{m/s}$ for a 13 mm thick MMC ceramic plate. Our goal is to estimate qualitatively when the characteristic damage mechanisms occur. Figures 8.3 and 8.4 show a contour plot of the damage as a function of velocity and the coefficient of restitution respectively. The coefficient of restitution is defined as $e = V_R/V_0$, where V_R is the projectiles rebound velocity and V_0 is its impact velocity. If $e = 1$ the collision is perfectly elastic, and deviations from unity indicate the onset of plasticity. Strictly speaking, $e = 1$ implies an elastic collision only if the plate does not move, here this is approximately satisfied since the projectile's mass is much smaller than the plate's mass. The plate's velocity after impact was $\approx 1.6\,\mathrm{m/s}$ when the projectile's impact velocity was $800\,\mathrm{m/s}$.

For low velocities ($V = 10\,\&\,50\,\mathrm{m/s}$) neither the ceramic or projectile becomes damaged, and the high coefficient of restitution indicates that the collision is close to being perfectly elastic. As the velocity increases to $V = 100\,\mathrm{m/s}$ we observe small hints of the beginning of cone formation close to the surface. However, the primary damage occurs inside of the ceramic, in the form of a median crack. The median crack is connected to damage contours that take the form of lateral and radial cracks. Continuing to increase the projectile velocity results in that the cracks increase in severity, and that the coefficient of restitution decreases. For $V = 200\,\mathrm{m/s}$, we obtain a complete primary cone crack, and for $V = 300\,\mathrm{m/s}$ we obtain a secondary cone crack. For even higher velocities the projectile begins to deform, and eventually the plate becomes bent in addition to experiencing significant interior damage.

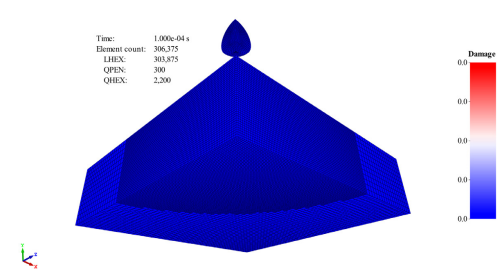

(a) $V = 10\,\mathrm{m/s}$

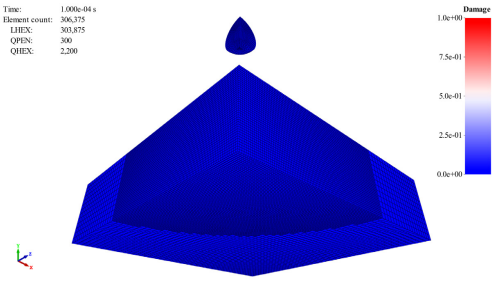

(b) $V = 50\,\mathrm{m/s}$

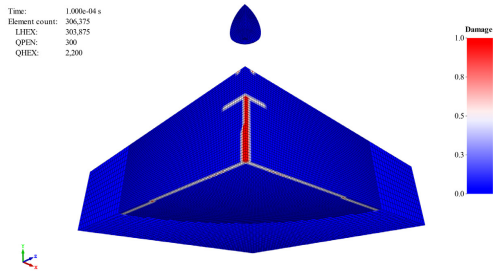

(c) $V = 100\,\mathrm{m/s}$

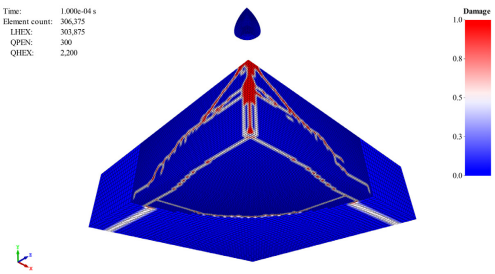

(d) $V = 200\,\mathrm{m/s}$

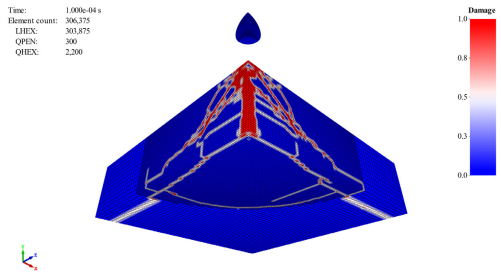

(e) $V = 300\,\mathrm{m/s}$

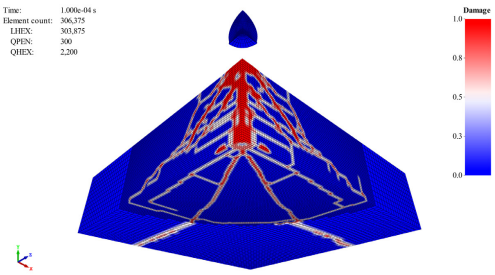

(f) $V = 400\,\mathrm{m/s}$

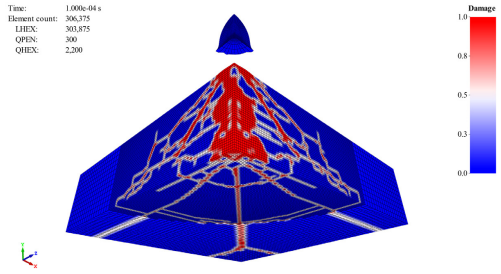

(g) $V = 500\,\mathrm{m/s}$

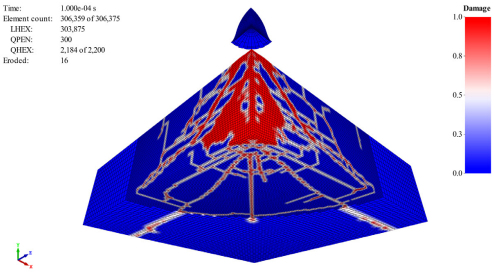

(h) $V = 600\,\mathrm{m/s}$

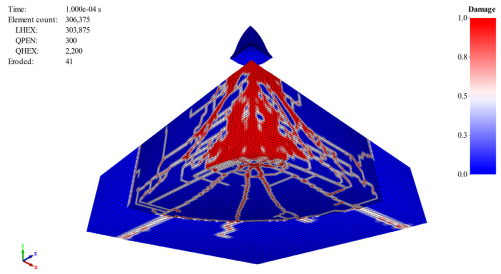

(i) $V = 700\,\mathrm{m/s}$

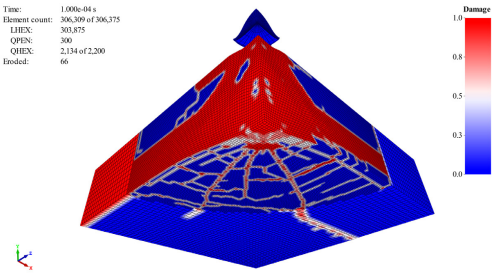

(j) $V = 800\,\mathrm{m/s}$

Figure 8.3 Damage to the MMC ceramic as a function of velocity.

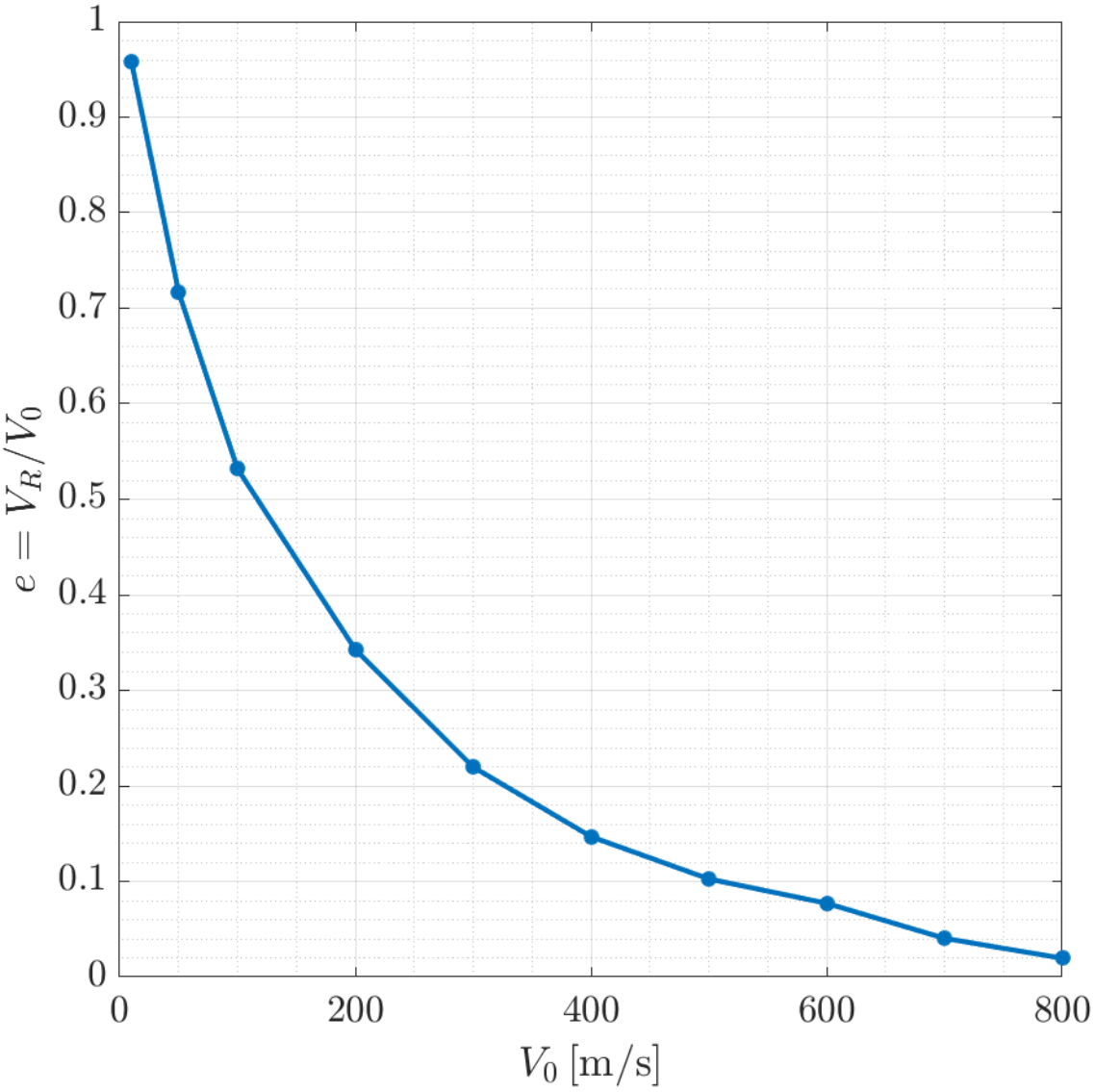

Figure 8.4 Coefficient of restitution as a function of velocity.

8.2 Symmetry

In Fig. 8.5 we compare the $v = 300\,\mathrm{m/s}$ impact of the MMC ceramic plate for the cases of quarter and zero symmetry. In the quarter symmetry case (left), the radial cracks initiates close to the symmetry planes, and one might therefore believe them to be a consequence of the quarter-symmetry boundary conditions. We explicitly tested this, by performing a calculation without any symmetry boundary conditions (right). The simulations utilizing quarter and zero symmetry are globally similar, with only minor differences to secondary cracks. The simulation with and without symmetry suggests that the application of symmetry boundary conditions does not substantially change the cracking pattern. Nevertheless, we do advise to use zero (alternatively half) symmetry conditions in the future to describe projectiles with finite pitch and yaw.

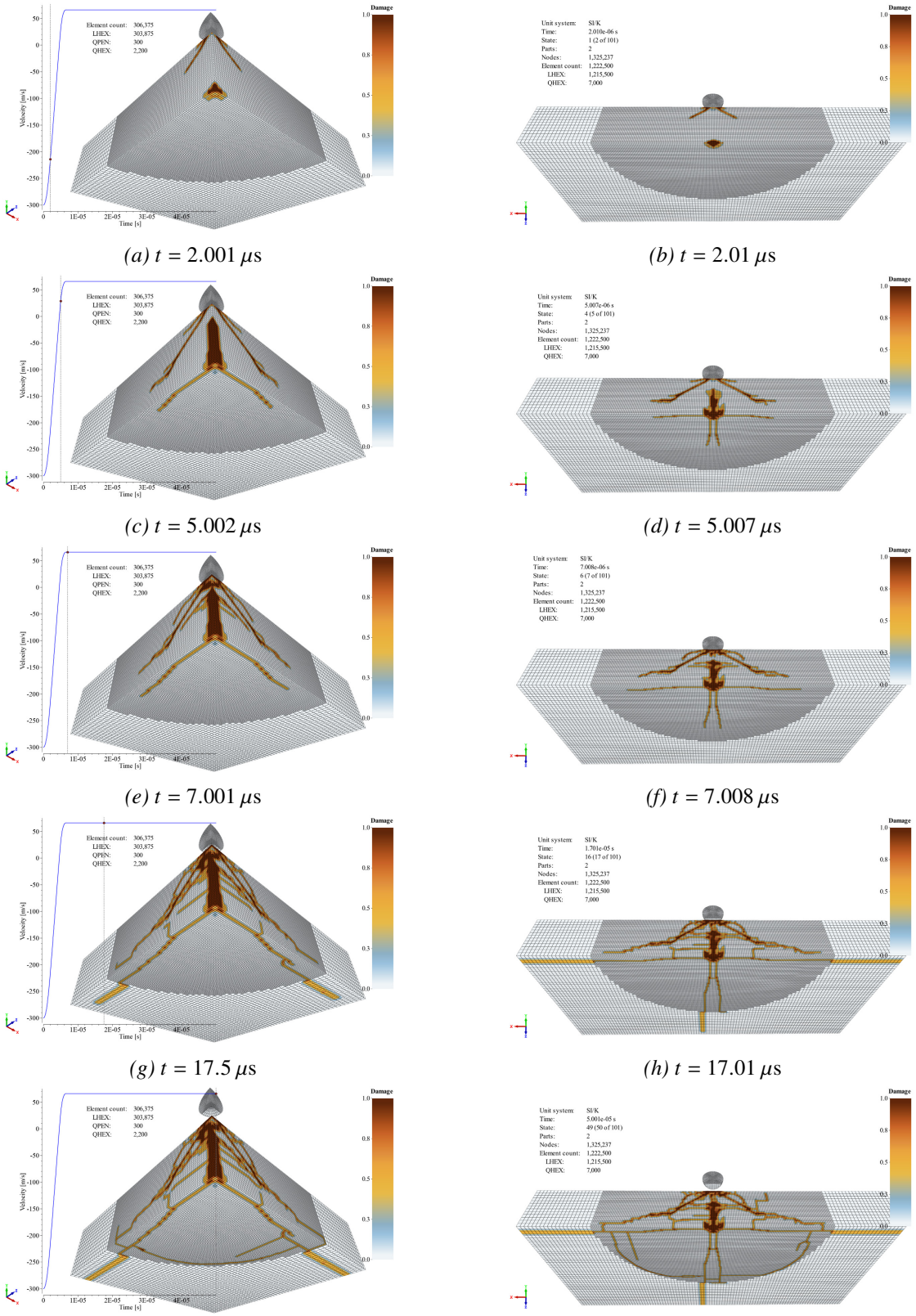

(a) $t = 2.001\ \mu s$ *(b)* $t = 2.01\ \mu s$

(c) $t = 5.002\ \mu s$ *(d)* $t = 5.007\ \mu s$

(e) $t = 7.001\ \mu s$ *(f)* $t = 7.008\ \mu s$

(g) $t = 17.5\ \mu s$ *(h)* $t = 17.01\ \mu s$

(i) $t = 50\ \mu s$ *(j)* $t = 50.01\ \mu s$

Figure 8.5 Comparing the crack development in the MMC ceramic as a function of time, for quarter (left) and full (right) symmetry.

8.3 Ceramic thickness

In Fig. 8.6 we consider a $v = 300\,\mathrm{m/s}$ projectile impacting a 9 mm, 13 mm, and 17 mm thick MMC ceramic. In the three simulations we have not used any symmetry boundary conditions. As is reasonable, when the thickness of the plate increases the numerical model predicts that the plate can sustain more damage, which is particularly evident by the reduction of radial cracks.

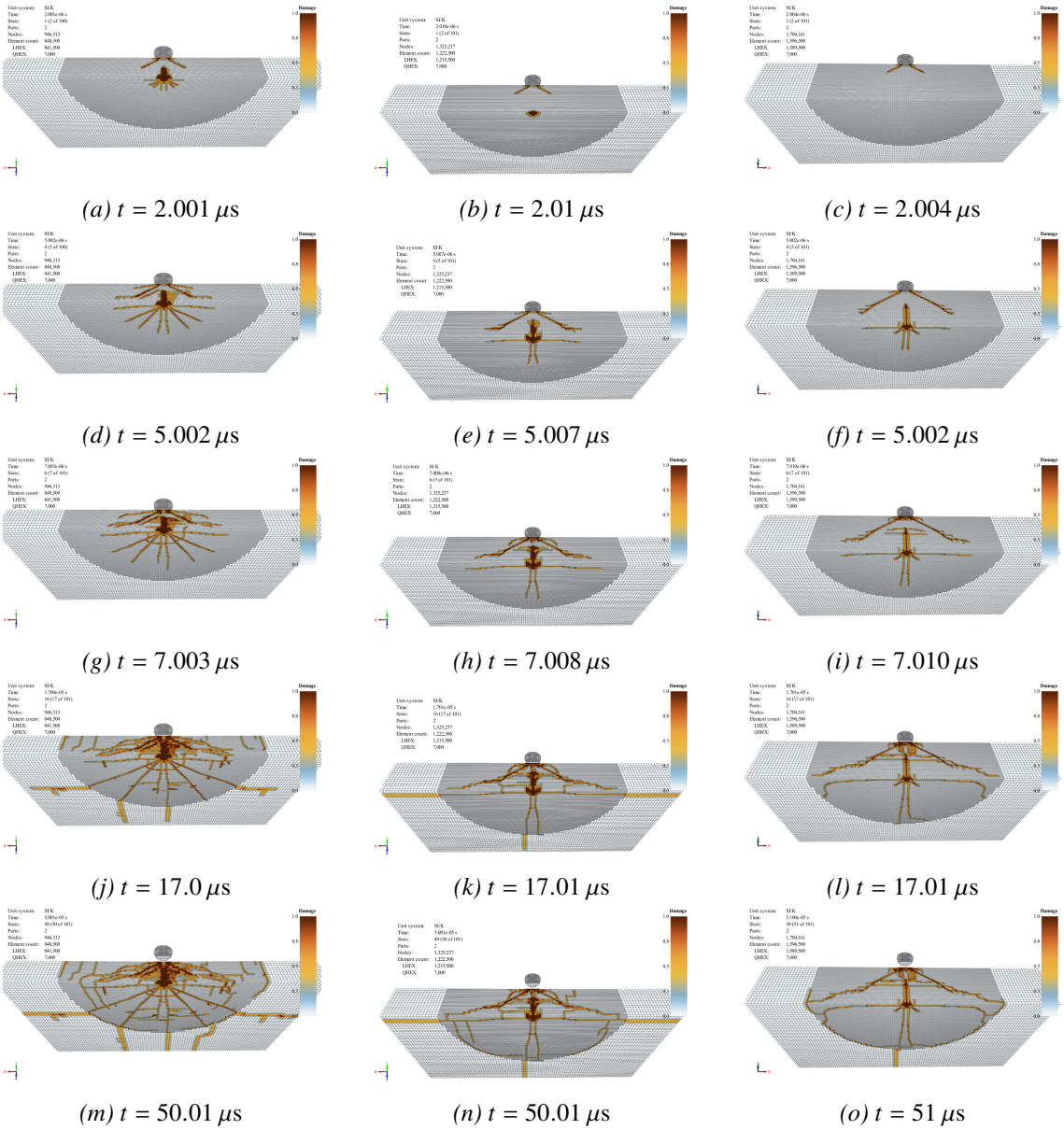

(a) $t = 2.001\,\mu\mathrm{s}$ *(b)* $t = 2.01\,\mu\mathrm{s}$ *(c)* $t = 2.004\,\mu\mathrm{s}$

(d) $t = 5.002\,\mu\mathrm{s}$ *(e)* $t = 5.007\,\mu\mathrm{s}$ *(f)* $t = 5.002\,\mu\mathrm{s}$

(g) $t = 7.003\,\mu\mathrm{s}$ *(h)* $t = 7.008\,\mu\mathrm{s}$ *(i)* $t = 7.010\,\mu\mathrm{s}$

(j) $t = 17.0\,\mu\mathrm{s}$ *(k)* $t = 17.01\,\mu\mathrm{s}$ *(l)* $t = 17.01\,\mu\mathrm{s}$

(m) $t = 50.01\,\mu\mathrm{s}$ *(n)* $t = 50.01\,\mu\mathrm{s}$ *(o)* $t = 51\,\mu\mathrm{s}$

Figure 8.6 Comparing the crack development in the MMC ceramic as a function of time, for a 9 mm (left), 13 mm (middle), and 17 mm (right) thick plate.

8.4 Isotropy and mesh sensitivity

In Sec. 7 we introduced the two material models (JH2 and MMC) that we have employed in Impetus. The following analysis applies to both material models, but we will provide examples using MMC as it is seems to work better than JH2. In Fig. 8.7 we consider a geometry, where the ceramic plate is divided into linear cubic hexagonal elements. Furthermore, the ceramic plate is partitioned into cylindrical sub-regions where the mesh is refined. In all cases we observe the usual crack formation: firstly the cone crack initiates, secondly the quasi-plastic zone, thirdly radial cracking, and finally lateral cracking. The cone crack appears to be relatively mesh independent, in the sense that the circular crack on the back of the ceramics plate does not significantly change radius. The resolution of the lateral cracks inside the cone become better as the refinement increases. However, the radial cracks appear to be mesh dependent. In a previous FFI publication [2] the same conclusion was reached by comparing a Cartesian and Polar mesh. In short, the number of radial cracks and their direction depends on the element size and the mesh symmetries.

To the best of our knowledge, the underlying physical reason for why this occurs and how it potentially can be avoided was not reported at the time. The most likely mechanism is that both the material models and mesh (if very fine) are isotropic. Consequently, the radial cracks have no preferential direction and will form in seemingly arbitrary directions based on small numerical differences (rounding errors, point of impact, mesh structure, etc.). To obtain a physically meaningful mesh convergence, one possible solution is to introduce anisotropy in some form.

One physical way of introducing anisotropy is to introduce defects into the ceramic. Such a solution has been suggested [36] with successful application [37] for the problem of blast loading on glass windows. At the time of writing, the role defects play in crack formation in ceramics under ballistic impact is relatively unexplored. The core idea is rather simple. The ceramic plate is populated by initial damage and defects picked from a statistical distribution. Upon ballistic loading, the cracks will tend to propagate toward the defects due to the reduced material strength. An advantage by using defects to introduce anisotropy is that the simulation more closely resembles a real ceramic plate, which has its own initial damage and defects due to the production process.

An objection to introducing defects might be that it will be impossible to obtain a one-to-one correspondence between the defects in the simulated and real ceramic plate. This is of course true, but the introduction of defects will on average mean that the strength of the simulated ceramic will be reduced and may therefore also affect more global properties such as the cone formation. Another option is to perform a Monte-Carlo simulation over many disorder configurations to obtain a statistical distribution of an ”average” real ceramic plate.

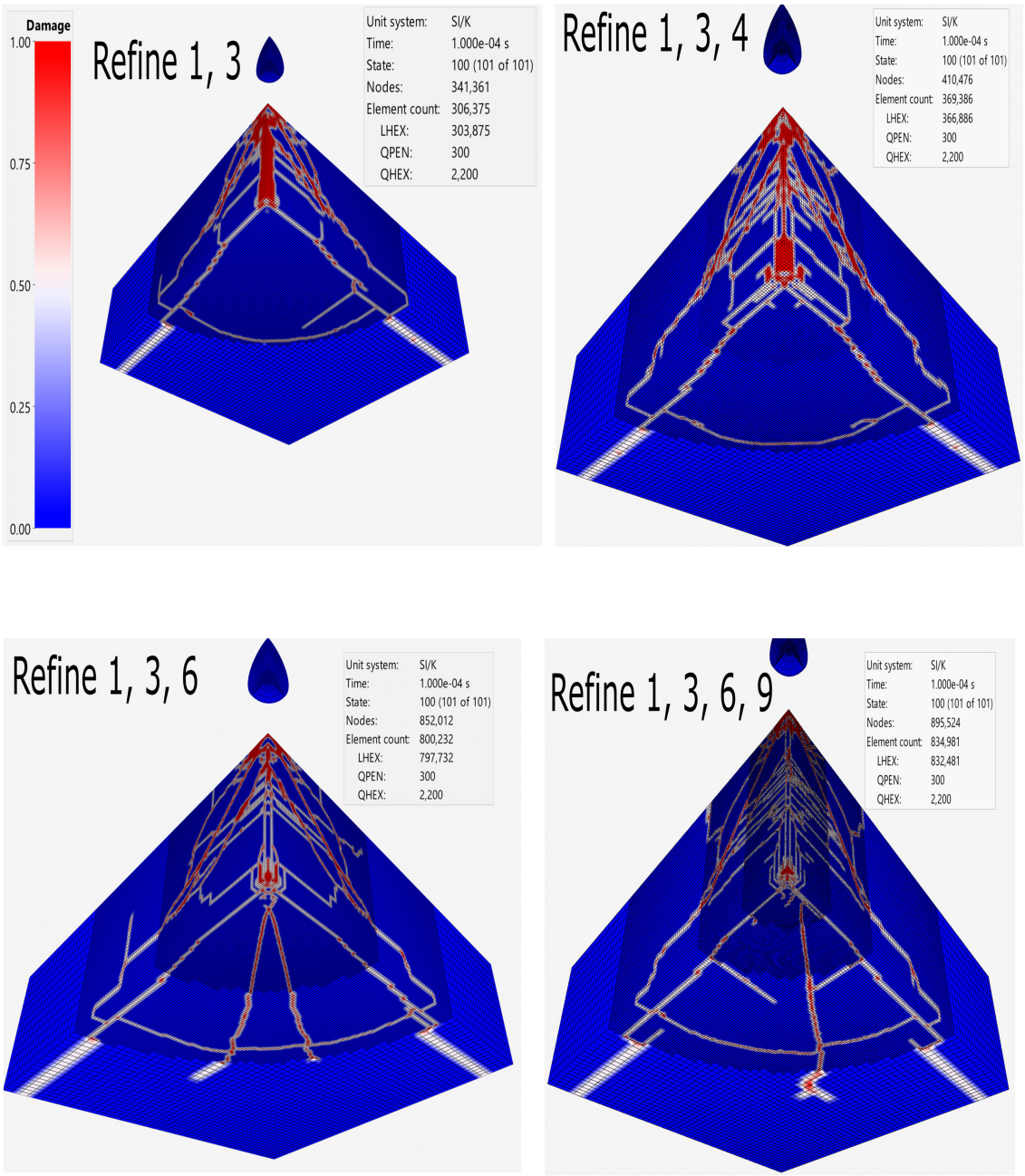

Figure 8.7 Crack formation as a function of increased mesh refinement. The MMC ceramic is divided into different regions. The regions close to the point of impact has a high degree of refinement.

9 Conclusion and outlook

The goal of this report was to investigate the physics describing the processes which determine whether or not a projectile will defeat a ceramic armor system. In practice there are two (natural) ways to tackle the problem, either analytically starting from first principles, or numerically by utilizing well-known and newly developed material models. Herein we have presented an investigation into both approaches.

The first part of this report consists of a detailed literature study of the simplest phenomena involved in ballistic impact phenomena. Due to the brittle nature of ceramics, we have primarily focused on the quasistatic and dynamic Hertzian theory, which applies to elastic materials. We have also gone beyond, and included non-linear plasticity effects inspired by Yoffe's seminal work. The analytical models, in their current form, effectively captures the observed experimental crack patterns. In addition, the model predicts how the relevant cracks can be mitigated through specific boundary conditions to create improved armor. We also discuss the advantages and limitations of the model, the most prominent being that it is unable to capture the relevant shockwave dynamics. Our review indicates that the analytical models may be suitable as building blocks in the future development of either a new ceramic material model or a simplified ballistic loading history, which may be included in relevant finite element codes such as Impetus, LS-Dyna or Abaqus.

In the report's second part, we investigate commercial solutions to the ballistic impact problem. All the finite element simulations have been performed in the program Impetus Afea. Conventionally, the Johnson-Holmquist 2 (JH2) model is the go-to model when describing ceramics. Here, we explicitly demonstrate that there exists a large range of parameter values in the open literature when using the JH2 model to describe a single material. This may indicate that the JH2 model suffers from parameter tuning, where each parameter set only fit one type of experiment. In other words, there is little consensus (in the open literature) in how to utilize the JH2 model to correctly describe an alumina ceramic system. With this in mind, the Impetus team has recently developed their own ceramic model, which they have named the MMC model. Herein we have compared the MMC and JH2 models, and used the MMC model to describe relevant experiments. In general, we find that the MMC model outperforms the JH2 model significantly, with regard to describing the cracking mechanisms of ceramics. Concretely, the MMC model is able to describe the cone, median, lateral, and radial cracks accurately during both the loading and unloading phase. The cracking processes are captured, even when varying physical parameters such as the projectile velocity and target thickness. We have looked into the issues of symmetry boundary conditions, isotropy, and mesh sensitivity. In general, there are dependencies in the minor cracks, while the cone crack is relatively unaffected. At this early stage, the artificial numerical crack dependencies are unimportant for the overall crack picture which we attempt to capture.

In the future we plan to continue the development of the ballistic impact problem through both approaches presented herein. For the development of the in-house material model the most pressing issue is to find a way to describe the relevant shock dynamics appropriately. In order to calibrate the MMC model we need to perform several in-house experiments at different scales to ensure that we find a more universal parameter set appropriate for alumina. We also aim to eventually be able to describe the deformation of more realistic projectiles with metallic cores. In this case it is necessary to perform impact experiments where the material properties of the target is well known, and the projectile is treated as the unknown.

References

[1] D. B. Rahbek and B. B. Johnsen. Dynamic behaviour of ceramic armour systems. Technical Report 15/01485, Norwegian Defence Reseach Establishment (FFI), 2015.

[2] D. B. Rahbek. Modelling impact of an armour piercing round onto ceramics using IMPETUS Afea Solver. Technical Report 17/00971, Norwegian Defence Reseach Establishment (FFI), 2017.

[3] D. B. Rahbek, J. W. Simons, B. B. Johnsen, T. Kobayashi, and D. A. Shockey. Effect of composite covering on ballistic fracture damage development in ceramic plates. *International Journal of Impact Engineering*, 99:58–68, 2017.

[4] H. Hertz. *Miscellaneous Papers*. Macmillan, 1896.

[5] B. R. Lawn. Indentation of ceramics with spheres: A century after hertz. *Journal of the American Ceramic Society*, 81(8):1977–1994, 1998.

[6] K. Osnes, J. K. Holmen, O. S. Hopperstad, and T. Børvik. Fracture and fragmentation of blast-loaded laminated glass: An experimental and numerical study. *International Journal of Impact Engineering*, 132:103334, 2019.

[7] K. Osnes, S. Dey, O. S. Hopperstad, and T. Børvik. On the dynamic response of laminated glass exposed to impact before blast loading. *Experimental Mechanics*, 59(7):1033–1046, Sep 2019.

[8] K. Osnes, J. K. Holmen, T. Grue, and T. Børvik. Perforation of laminated glass: An experimental and numerical study. *International Journal of Impact Engineering*, 156:103922, 2021.

[9] M. T. Huber. Zur Theorie der Berührung fester elastischer Körper. *Annalen der Physik*, 319(6):153–163, 1904.

[10] E. Winkler. *Die Lehre von der Elastizität und Festigkeit: 1. Teil*. Salzwasser-Verlag GmbH, 2020.

[11] F. C. Frank and B. R. Lawn. On the theory of Hertzian fracture. *Proceedings of the Royal Society of London. Series A. Mathematical and Physical Sciences*, 299(1458):291–306, 1967.

[12] A. C. Fischer-Cripps. *Elastic Indentation Stress Fields*, pages 77–100. Springer US, Boston, MA, 2007.

[13] K. L. Johnson. *Contact Mechanics*. Cambridge University Press, 1985.

[14] E. H. Yoffe. Elastic stress fields caused by indenting brittle materials. *Philosophical Magazine A*, 46(4):617–628, 1982.

[15] M. M. Chaudhri. Chapter 70 - dislocations and indentations. In F. R. N. Nabarro and J. P. Hirth, editors, *Dislocations in Solids*, volume 12 of *Dislocations in Solids*, pages 447–550. Elsevier, 2004.

[16] J. Boussinesq. *Application des potentiels à l'étude de l'équilibre et du mouvement des solides élastiques: principalement au calcul des déformations et des pressions que produisent, dans ces solides, des efforts quelconques exercés sur une petite partie de leur surface ou de leur intérieur : mémoire suivi de notes étendues sur divers points de physique, mathematique et d'analyse*. Mémoires de la société des sciences, de l'agriculture et des arts de Lille. Gauthier-Villars, 1885.

[17] A. E. H. Love. *A Treatise on the Mathematical Theory of Elasticity*. Cambridge University Press, 2013.

[18] D. B. Marshall. Geometrical effects in elastic/plastic indentation. *Journal of the American Ceramic Society*, 67(1):57–60, 1984.

[19] D. B. Marshall, B. R. Lawn, and A.G. Evans. Elastic/plastic indentation damage in ceramics: The lateral crack system. *Journal of the American Ceramic Society*, 65(11):561–566, 1982.

[20] R. F. Cook and G. M. Pharr. Direct observation and analysis of indentation cracking in glasses and ceramics. *Journal of the American Ceramic Society*, 73(4):787–817, 1990.

[21] G. Feng, S. Qu, Y. Huang, and W.D. Nix. An analytical expression for the stress field around an elastoplastic indentation/contact. *Acta Materialia*, 55(9):2929–2938, 2007.

[22] G. Feng, S. Qu, Y. Huang, and W. D. Nix. A quantitative analysis for the stress field around an elastoplastic indentation/contact. *Journal of Materials Research*, 24(3):704–718, Mar 2009.

[23] P. Lundberg, R. Renström, and B. Lundberg. Impact of metallic projectiles on ceramic targets: transition between interface defeat and penetration. *International Journal of Impact Engineering*, 24(3):259–275, 2000.

[24] L Westerling, P Lundberg, and B Lundberg. Tungsten long-rod penetration into confined cylinders of boron carbide at and above ordnance velocities. *International Journal of Impact Engineering*, 25(7):703–714, 2001.

[25] P. Lundberg and B. Lundberg. Transition between interface defeat and penetration for tungsten projectiles and four silicon carbide materials. *International Journal of Impact Engineering*, 31(7):781–792, 2005.

[26] P. Lundberg, R. Renström, and B. Lundberg. Impact of conical tungsten projectiles on flat silicon carbide targets: Transition from interface defeat to penetration. *International Journal of Impact Engineering*, 32(11):1842–1856, 2006.

[27] G. Toussaint and I. Polyzois. Steel spheres impact on alumina ceramic tiles: Experiments and finite element simulations. *International Journal of Applied Ceramic Technology*, 16(6):2131–2152, 2019.

[28] Impetus Afea Solver. `http://www.impetus-afea.com/.` Accessed: 06.07.2023.

[29] G. R. Johnson and W. H. Cook. In: Proceedings of seventh international symposium on ballistics. *A Constitutive Model and Data for Metals Subjected to Large Strains, High Strain Rates and High Temperatures*, 1983.

[30] G. R. Johnson and W. H. Cook. Fracture characteristics of three metals subjected to various strains, strain rates, temperatures and pressures. *Engineering Fracture Mechanics*, 21:31–48, 1985.

[31] D. S. Cronin, K. Bui, C. Kaufmann, G. McIntosh, and T. Berstad. Implementation and Validation of the Johnson-Holmquist Ceramic Material Model in LS-Dyna. In *4th European LS-Dyna Users Conference*, 2003.

[32] L. Westerling. *Interaction of Cylindrical Penetrators with Ceramic and Electromagnetic Armour*. PhD thesis, Uppsala University, Faculty of Science and Technology, 2013.

[33] A. Tasdemirci and I.W. Hall. Numerical and experimental studies of damage generation in multi-layer composite materials at high strain rates. *International Journal of Impact Engineering*, 34(2):189–204, 2007.

[34] J. Ning, H. Ren, T. Guo, and P. Li. Dynamic response of alumina ceramics impacted by long tungsten projectile. *International Journal of Impact Engineering*, 62:60–74, 2013.

[35] P. Lundberg. *Interface Defeat and Penetration: Two Modes of Interaction between Metallic Projectiles and Ceramic Targets*. PhD thesis, Uppsala University, Faculty of Science and Technology, 2004.

[36] D. Z. Yankelevsky. Strength prediction of annealed glass plates – A new model. *Engineering Structures*, 79:244–255, 2014.

[37] K. Osnes. *Monolithic and laminated glass under extreme loading: Experiments, modelling and simulations*. PhD thesis, Norwegian University of Science and Technology, Department of Structural Engineering, 2019.

[38] A. Flamant. Sur la répartition des pressions dans un solide rectangulaire chargé transversalement. *Comptes Rendus des Séances de l'Académie des Sciences*, 114:1465–1468, 1892.

[39] I. N. Sneddon. Boussinesq's problem for a rigid cone. *Mathematical Proceedings of the Cambridge Philosophical Society*, 44(4):492–507, 1948.

[40] I. N. Sneddon. Boussinesq's problem for a flat-ended cylinder. *Mathematical Proceedings of the Cambridge Philosophical Society*, 42(1):29–39, 1946.

[41] J. W. Harding and I. N. Sneddon. The elastic stresses produced by the indentation of the plane surface of a semi-infinite elastic solid by a rigid punch. *Mathematical Proceedings of the Cambridge Philosophical Society*, 41(1):16–26, 1945.

[42] M. Barquins and D. Maugis. Adhesive contact of axisymmetric punches on an elastic half-space: The modified hertz-huber's stress tensor for contacting spheres. *J. Mec. Theor. Appl.*, 1:331–357, 1982.

A Analytical solutions for the Hertzian stress tensor

In this section we summarize various solutions for the induced stress fields occurring when a load is applied to a semi-infinite half space. The half space is characterized by a Poisson ratio ν, and that it behaves elastically. By using the superposition principle the more complex indenter solutions can be built from the fundamental solutions, the most important being the point contact. The most relevant indenters for ballistic impact are the cylindrical (flat punch) indenter, the spherical indenter, and the conical indenter. In all cases the stress tensor is decomposed into a cylindrical polar coordinate system (r, θ, z). The z-coordinate points into the semi-infinite plane. A more detailed analysis can be found in [12].

A.1 Fundamental solutions

In this section we introduce the analytical expression for the stress field induced in a semi-infinite plane by the simplest types of surface loading. The strength of the loading is P.

A.1.1 Point contact

The stresses within a solid loaded by a point contact were first calculated by Boussinesq [16]. In cylindrical polar coordinates the solution is

$$\begin{aligned}
\sigma_{rr} &= \frac{P}{2\pi}\left\{(1-2\nu)\left[\frac{1}{r^2}-\frac{z}{r^2\left(r^2+z^2\right)^{1/2}}\right]-\frac{3r^2z}{\left(r^2+z^2\right)^{5/2}}\right\} \\
\sigma_{\theta\theta} &= \frac{P}{2\pi}(1-2\nu)\left\{-\frac{1}{r^2}+\frac{z}{r^2\left(r^2+z^2\right)^{1/2}}+\frac{z}{\left(r^2+z^2\right)^{3/2}}\right\} \\
\sigma_{zz} &= -\frac{3P}{2\pi}\frac{z^3}{\left(r^2+z^2\right)^{5/2}} \\
\tau_{rz} &= -\frac{3P}{2\pi}\frac{rz^2}{\left(r^2+z^2\right)^{5/2}}
\end{aligned} \tag{A.1}$$

A.1.2 Line contact

The stress field induced in the material by a infinite line load was first derived analytically by Flamant [38]. Due to the symmetry of the problem, the stress field always points radially from the point of interest to the point of contact. In two-dimensional polar coordinates the induced stress field is

$$\begin{aligned}
\sigma_{rr} &= -\frac{2P}{\pi}\frac{\cos\theta}{r} \\
\sigma_{\theta\theta} &= \tau_{r\theta} = 0.
\end{aligned} \tag{A.2}$$

The stress singularity at $r = 0$ is in practice avoided by plastic yielding, which spreads the load over a small finite area.

A.2 Practical solutions for indenters

In this section we introduce the analytical expression for the stress field induced in a semi-infinite plane by indenters of practical interest. The stresses are normalized with respect to the mean contact pressure $p_0 = P/\pi a^2$.

A.2.1 Spherical indenter

The components of the Cauchy stress tensor for the Hertzian contact between a semi-infinite plane and spherical indenter is

$$\begin{aligned}
\frac{\sigma_{rr}(r,z;a)}{p_0} &= \frac{3}{2}\left\{\frac{1-2\nu}{3}\left(\frac{a}{r}\right)^2\left[1-\left(\frac{z}{\sqrt{u}}\right)^3\right]+\left(\frac{z}{\sqrt{u}}\right)^3\frac{a^2u}{u^2+a^2z^2}\right.\\
&\qquad\left.+\left(\frac{z}{\sqrt{u}}\right)\left[\frac{1-\nu}{a^2+u}u+(1+\nu)\,\frac{\sqrt{u}}{a}\arctan\left(\frac{a}{\sqrt{u}}\right)-2\right]\right\},\\
\frac{\sigma_{\theta\theta}(r,z;a)}{p_0} &= -\frac{3}{2}\left\{\frac{1-2\nu}{3}\left(\frac{a}{r}\right)^2\left[1-\left(\frac{z}{\sqrt{u}}\right)^3\right]\right.\\
&\qquad\left.+\left(\frac{z}{\sqrt{u}}\right)\left[2\nu+\frac{1-\nu}{a^2+u}u-(1+\nu)\,\frac{\sqrt{u}}{a}\arctan\left(\frac{a}{\sqrt{u}}\right)\right]\right\},\\
\frac{\sigma_{zz}(r,z;a)}{p_0} &= -\frac{3}{2}\left(\frac{z}{\sqrt{u}}\right)^3\frac{a^2u}{u^2+a^2z^2},\\
\frac{\tau_{rz}(r,z;a)}{p_0} &= -\frac{3}{2}\frac{rz^2}{u^2+a^2z^2}\frac{a^2\sqrt{u}}{u+a^2},
\end{aligned} \tag{A.3}$$

where

$$u(r,z;a) = \frac{1}{2}\left(r^2+z^2-a^2+\sqrt{\left(r^2+z^2-a^2\right)^2+4a^2z^2}\right). \tag{A.4}$$

Finally, note that when evaluating the stress-tensor components at the surface it is often useful to know the following limit

$$\left(\frac{z}{\sqrt{u}}\right)_{z=u=0} = \sqrt{1-(r/a)^2}. \tag{A.5}$$

A.2.2 Conical indenter

The stress field due to a conical indenter [39] is of interest because, i) it approximates the indenter used in various hardness test, and ii) it can be used as a model for a sharp projectile. The stress field

induced in the specimen can be expressed using cylindrical polar coordinates as

$$\begin{aligned}
\frac{\sigma_{zz}}{p_0} &= -\left(J_1^0 + \frac{z}{a}J_2^0\right), \\
\frac{\sigma_{\theta\theta}}{p_0} &= -\left\{2\nu J_1^0 + \frac{a}{r}\left[(1-2\nu)\,J_0^1 - \frac{z}{a}J_1^1\right]\right\}, \\
\frac{\sigma_{rr}}{p_0} &= -\frac{2\left(1-\nu^2\right)}{1-\nu}J_1^0 - \frac{\sigma_{zz}}{p_0} - \frac{\sigma_{\theta\theta}}{p_0}, \\
\tau_{rz} &= -\frac{z}{a}J_2^1.
\end{aligned} \tag{A.6}$$

We have here introduced the following auxiliary functions:

$$\begin{aligned}
J_0^1 &= \frac{1}{2}\left[\frac{r}{a}J_1^0 + \frac{a}{r}\left(1 - R\sin\phi\right) - \frac{z}{a}J_1^1\right], \\
J_1^0 &= \frac{1}{2}\ln\left\{\frac{R^2 + 2R\left(1+z^2/a^2\right)^{1/2}\cos\left(\theta-\phi\right) + 1 + z^2/a^2}{\left[z/a + \left(r^2/a^2 + z^2/a^2\right)^{1/2}\right]^2}\right\}, \\
J_1^1 &= \frac{a}{r}\left[\left(\frac{r^2}{a^2} + \frac{z^2}{a^2}\right)^{1/2} - R\cos\phi\right], \\
J_2^0 &= \left(\frac{r^2}{a^2} + \frac{z^2}{a^2}\right)^{-1/2} - \frac{\cos\phi}{R}, \\
J_2^1 &= \frac{a}{r}\left[\frac{\left(1+z^2/a^2\right)^{1/2}}{R}\cos\left(\theta-\phi\right) - \frac{z}{a}\left(\frac{r^2}{a^2} + \frac{z^2}{a^2}\right)^{-1/2}\right], \\
\tan 2\phi &= 2\frac{z}{a}\left(\frac{r^2}{a^2} + \frac{z^2}{a^2} - 1\right)^{-1}, \\
\tan\theta &= \frac{a}{z}, \\
R &= \left[\left(\frac{r^2}{a^2} + \frac{z^2}{a^2} - 1\right)^2 + 4\frac{z^2}{a^2}\right]^{1/2}.
\end{aligned}$$

A.2.3 Cylindrical (flat punch) indenter

The stress field due to a cylindrical flat punch indenter has been determined analytically several authors [40, 41, 42]. Inside the specimen the stress distribution in cylindrical polar coordinates is

$$\begin{aligned}
\frac{\sigma_{rr}}{p_0} &= -\frac{1}{2}\left\{J_1^0 - z/aJ_2^0 - (1-2\nu)\,\frac{a}{r}J_0^1 + \frac{z}{r}J_1^1\right\}, \\
\frac{\sigma_{\theta\theta}}{p_0} &= -\frac{1}{2}\left\{2\nu J_1^0 + (1-2\nu)\,\frac{a}{r}J_0^1 - \frac{z}{r}J_1^1\right\}, \\
\frac{\sigma_{zz}}{p_0} &= -\frac{1}{2}\left\{J_1^0 + \frac{z}{a}J_2^0\right\}, \\
\frac{\tau_{rz}}{p_0} &= -\frac{1}{2}\frac{z}{a}J_2^1.
\end{aligned} \tag{A.7}$$

Again, to lighten the notation it is necessary to define the following auxiliary functions:

$$
\begin{aligned}
&J_0^1 = \frac{a}{r}\left(1 - R^{1/2}\sin\frac{\phi}{2}\right), \\
&J_1^0 = R^{-1/2}\sin\frac{\phi}{2}, && J_1^1 = \left(1+\frac{z^2}{a^2}\right)^{1/2}\frac{a}{r}R^{-1/2}\sin\left(\theta-\frac{\phi}{2}\right), \\
&J_2^0 = \left(1+\frac{z^2}{a^2}\right)^{1/2} R^{-3/2}\sin\left(\frac{3\phi}{2}-\theta\right), && J_2^1 = \frac{r}{a}R^{-3/2}\sin\frac{3\phi}{2}, \\
&\tan\phi = 2\frac{z}{a}\left(\frac{r^2}{a^2}+\frac{z^2}{a^2}-1\right)^{-1}, && \tan\theta = \frac{a}{z}, \\
&R = \left[\left(\frac{r^2}{a^2}+\frac{z^2}{a^2}-1\right)^2 + 4\frac{z^2}{a^2}\right]^{1/2}.
\end{aligned}
$$

A.3 Diagonalization of the Cauchy stress tensor

Due to the azimuthal symmetry, the Cauchy stress tensor in the substrate becomes particularly simple in cylindrical coordinates

$$
\boldsymbol{\sigma} = \begin{bmatrix} \sigma_{rr} & \tau_{rz} & 0 \\ \tau_{rz} & \sigma_{zz} & 0 \\ 0 & 0 & \sigma_{\theta\theta} \end{bmatrix}. \tag{A.8}
$$

The stress tensor is diagonalized by a rotation in the (r, z)-plane of the form

$$
\boldsymbol{\sigma}' = \boldsymbol{Q}^T\boldsymbol{\sigma}\boldsymbol{Q}, \tag{A.9}
$$

with the rotation matrix

$$
\boldsymbol{Q} = \begin{bmatrix} \cos\phi^* & -\sin\phi^* & 0 \\ \sin\phi^* & \cos\phi^* & 0 \\ 0 & 0 & 1 \end{bmatrix}, \tag{A.10}
$$

and rotation angle

$$
\tan 2\phi^* = \frac{2\tau_{rz}}{\sigma_{rr}-\sigma_{zz}}. \tag{A.11}
$$

The principal stresses (eigenvalues) and corresponding principal directions (eigenvectors) are

$$
\begin{aligned}
&\sigma_1 = \frac{1}{2}\left((\sigma_{rr}+\sigma_{zz}) + \sqrt{\left[\frac{1}{2}(\sigma_{rr}-\sigma_{zz})\right]^2+\tau_{rz}^2}\right), && V_1 = (\cos\phi^*, \sin\phi^*, 0)\,, \\
&\sigma_2 = \sigma_{\theta\theta}, && V_2 = (0,0,1)\,, \\
&\sigma_3 = \frac{1}{2}\left((\sigma_{rr}+\sigma_{zz}) - \sqrt{\left[\frac{1}{2}(\sigma_{rr}-\sigma_{zz})\right]^2+\tau_{rz}^2}\right), && V_3 = (-\sin\phi^*, \cos\phi^*, 0)\,.
\end{aligned} \tag{A.12}
$$

B Input files in Impetus

B.1 Characteristic JH2 simulation

- The simulation was run on the IMPETUS Afea Solver (version 7.0.280).
- Used CPU memory: 36635 MB.
- Used GPU memory: 32870 MB.
- Total run time 6h:57m:34s.

```
*UNIT_SYSTEM
SI
*PARAMETER
%R = 0.003175 #Projectile radius 3.175 mm
%H = 0.013 #Target thickness 13 mm
%L = 0.1016
*TIME
0.0001465
# Projectile
*COMPONENT_SPHERE #component-id 1, part-id 1
"Sphere"
1, 1, 4
0, 0, %R+0.1*%R, %R
*CHANGE_P-ORDER #Make sphere elements higher order
P, 1, 3
*SMOOTH_MESH #Make sphere mesh more smooth
P, 1, 45
*MAT_JC #Steel material, mid = 1, Using eos_gruneisen, damage property??
"Projectile steel material"
1,7800, 210e9, 0.3, , , 1
2.4824e9, 1.4985e9, 0.19, 0.027, 0.66, 293.15, 1760.15, 1
476.97501
*EOS_GRUNEISEN
1, 1.578, 1.60
*PART
"Sphere"
1,1
*INITIAL_VELOCITY
P,1,0,0,-300
# Target material 1
*MAT_JH_CERAMIC #Material id 3
"Alumina plate material"
3, 3860, 90.16e9
2.139, 0.31, 0, 0.6, 0.6, 1, 0.2e9
2.79e9, 1.46e9, 1, 0.0025, 0.5, 130.95e9, 0, 0
2
*COMPONENT_BOX
```

```
"Target plate 1"
3, 3, 68, 68, 5
-%L/2, -%L/2, 0, %L/2, %L/2, -%H
*PART
"Target plate 1"
3, 3, , , , , 3
*GEOMETRY_PIPE
"Target refine"
1
0, 0, 2*%H, 0, 0, -2*%H, 10*%R
*REFINE
P, 3, 3, 1
*CHANGE_P-ORDER
"Target p-order"
P, 3, 3,1
*CONTACT
1
ALL, , ALL, , 0.03
*INITIAL_TEMPERATURE
ALL, , 100
*FUNCTION
100
293
*END
```

B.2 Characteristic MMC simulation

- The simulation was run on the IMPETUS Afea Solver (version 8.0.368).
- Used CPU memory: 7192 MB.
- Used GPU memory: 5911 MB.
- Total run time 0h:45m:8s.

```
*PARAMETER
tend = 1e-4    , "Termination time"
L    = 101.6e-3, "Side length of plate"
T    = 13.0e-3 , "Thickness of plate"
D    = 6.35e-3 , "Diameter of impacting sphere"
vel  = 300     , "Impact velocity"
dx   = 1e-3    , "Element side length"
#
*TIME
%tend
*UNIT_SYSTEM
SI
#
# AISI E 52100
```

```
#
*MAT_JC
"AISI E 52100"
1, 7800, 210e9, 0.3, 0, 1, 1
2.4824e9, 1.4985e9, 0.19, 0.027, 0.66, 293.15, 1760.15, 1
*PROP_THERMAL
1, 0, 476.97501, 0, 0.9, 293.15
*EOS_GRUNEISEN
1, 1.578, 1.60
#
# AL2O3 (based on SiC-calibration available as material object)
#
*PARAMETER
rho       = 3860      #3200   , "Density"
G         = 147.6e9   #198.3e9, "Shear modulus"
sig_c     = 5.75e9    #3.87e9 , "Uniaxial compressive strength"
sig_x     = 0.26e9    #6.32e9 , "Compressive strength at pressure x"
p_x       = -0.26e9/3 #2.39e9 , "Pressure x"
sig_cap   = 15.0e9 , "Cap on yield surface"
alpha     = 0.6    , "Failed-to-intact material strength ratio"
epsp_fail = 0.0    , "Effective plastic strain at failure"
yield     = 0.0    , "Type of yield surface (= 0.0 -> von Mises, = 1.0 -> Rankine)"
K         = 234.6e9   #225.5e9, "Bulk modulus"
beta      = 0.0    , "Parameter controlling the direction of plastic flow"
epsv_max  = 0.0    , "Cap on volumetric strain of bulking"
c         = 0.03   , "Strain rate parameter"
eps0      = 1.0e-2 , "Reference strain rate"
psi       = 0.0    , "Parameter controlling the rate dependency on the hydrostatic tens
d         = 1.0e3  , "Damping coefficient"
d_dec     = 0.0    , "Damping decay coefficient"
*MAT_MMC
"AL2O3"
2, %rho, %G
%sig_c, %sig_x, %p_x, %sig_cap, %alpha, %epsp_fail, %yield
%K, %beta, %epsv_max, %c, %eps0, %psi, %d, %d_dec
#
*COMPONENT_SPHERE
"Projectile"
1, 1, 10, 10, 0, 90
0, %D/2, 0, %D/2
*CHANGE_P-ORDER
P, 1, 2
*SMOOTH_MESH
P, 1, 30, 1
*COMPONENT_BOX
"Target"
```

```
2, 2, %L/(2*%dx), %T/%dx, %L/(2*%dx)
0, -%T, -%L/2, %L/2, 0, 0
*REFINE
P, 2, 3, 2
*GEOMETRY_PIPE
2, 0
0, -2*%T, 0, 0, %T, 0, 5*%D
#
*PART
1, 1, 0, 0, 0, 0, 3
2, 2, 0, 0, 0, 0, 3
*INITIAL_TEMPERATURE
ALL, 0, 0, 293.15
*INITIAL_VELOCITY
P, 1, 0, -%vel, 0
*CONTACT
1
ALL, 0, ALL, 0
*BC_SYMMETRY
ZX
*END
```

About FFI

The Norwegian Defence Research Establishment (FFI) was founded 11th of April 1946. It is organised as an administrative agency subordinate to the Ministry of Defence.

FFI's mission

FFI is the prime institution responsible for defence related research in Norway. Its principal mission is to carry out research and development to meet the requirements of the Armed Forces. FFI has the role of chief adviser to the political and military leadership. In particular, the institute shall focus on aspects of the development in science and technology that can influence our security policy or defence planning.

FFI's vision

FFI turns knowledge and ideas into an efficient defence.

FFI's characteristics

Creative, daring, broad-minded and responsible.

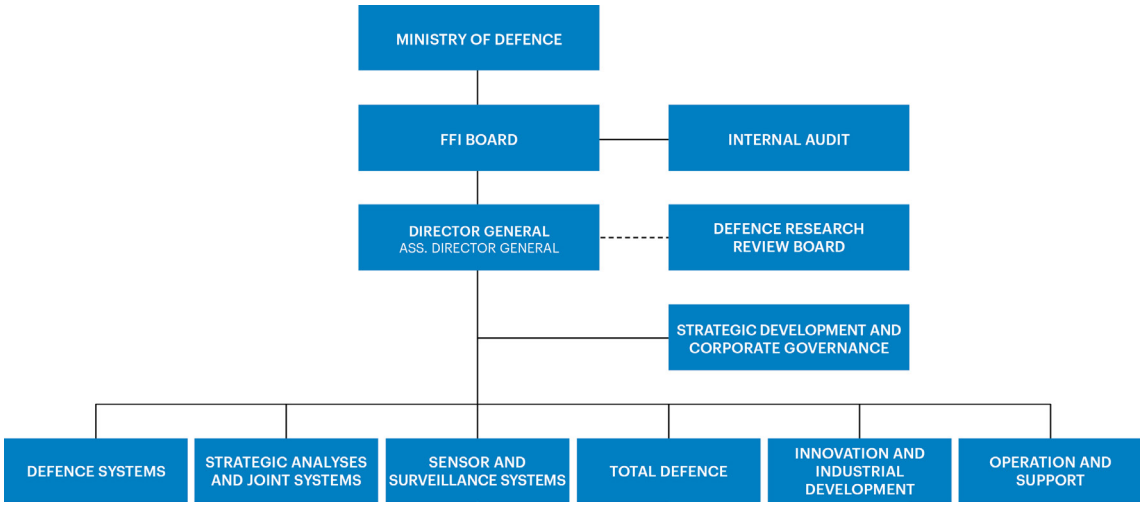

Forsvarets forskningsinstitutt (FFI)
Postboks 25
2027 Kjeller

Besøksadresse:
Kjeller: Instituttveien 20, Kjeller
Horten: Nedre vei 16, Karljohansvern, Horten

Telefon: 91 50 30 03
E-post: post@ffi.no
ffi.no

Norwegian Defence Research Establishment (FFI)
PO box 25
NO-2027 Kjeller
NORWAY

Visitor address:
Kjeller: Instituttveien 20, Kjeller
Horten: Nedre vei 16, Karljohansvern, Horten

Telephone: +47 91 50 30 03
E-mail: post@ffi.no
ffi.no/en